Design, Fabrication and Characterization of a Unipolar Charge Sensing Amorphous Selenium X-ray Detector

by

Zain Hussain Warsi

A thesis
presented to the University of Waterloo
in fulfillment of the
thesis requirement for the degree of
Master of Applied Science
in
Electrical and Computer Engineering

Waterloo, Ontario, Canada, 2023
© Zain Hussain Warsi 2023

Author's Declaration

I hereby declare that I am the sole author of this thesis. This is a true copy of the thesis, including any required final revisions, as accepted by my examiners.

I understand that my thesis may be made electronically available to the public.

Abstract

Amorphous Selenium is a direct conversion photoconductor that has been widely used in X-ray imaging applications. Due to its high spatial resolution A-Se plays an important role in breast cancer screening and diagnostics, allowing for the detection of small and subtle lesions. However, a-Se has poor collection efficiency due to low carrier mobility and charge trapping resulting from its amorphous structure. The trapped charges can cause memory artifacts, including photocurrent lag, which can persist for several seconds after the X-ray pulse has ended. As a result, a-Se is a challenging material for dynamic imaging applications that require high spatial resolution.

The research discussed in this thesis aims to investigate and address the temporal behavior of a-Se photoconductors, specifically the issue of lag, which can lead to image artifacts and degradation of image quality in dynamic imaging applications. The research involves the design of unipolar charge sensing detectors with pixel sizes of 20, 40, 80 and 150 microns to improve energy resolution and the temporal response compared to conventional a-Se detectors. Theoretical analysis and simulations are presented for the unipolar charge sensing detector including weighting potential, charge collection efficiency, pulse height spectroscopy and energy resolution which range from 5% to 2% . The work further discusses the fabrication process of the designed detector in the G2N lab at the university of Waterloo. It discusses the experimental results obtained and the challenges that were faced while fabricating the detector and how they can be overcome in the future.

Acknowledgements

First of all, I would like to thank my supervisors Professor Dr. Karim S. Karim and Dr. Ahmet Camlica for their guidance, encouragement and trust in me throughout this academic journey.

I would further extend my gratitude to Dr.Denny Lee whose advice was crucial for certain parts of the design and helped me understand core concepts of designing an X-ray photon counter.

I'm beholden to Dr. Bo Cui and Dr. William Wong for reviewing my thesis and being part of my Master degree seminar.

I'm highly indebted to my colleagues at the STAR Labs, University of Waterloo including Sahar Adnani, Abdollah Pil Ali, Ala Mohajer, Dr. Celal Con, Ahmad Lakhani, and Micheal Wright for the countless discussions and moral support which helped me get through the challenging times involving hours of pondering over the design and fabrication steps of my detector.

I am highly grateful to Richard Barber and Dr. Czhang-Ho Lee from the G2N Lab for the training and support they provided during the fabrication phase of my detector.

Finally, I would like to thank the University of Waterloo and the department of Electrical and Computer Engineering for giving me the opportunity to fulfill my dreams by granting me the Masters of Applied Science - Electrical and Computer Engineering Degree.

Dedication

This research work and thesis is dedicated to my loving parents Jaffer Hussain Warsi, Shagufta Warsi and to my grandparents Sajjad Hussain Warsi and Aisha Warsi whose love, support and blessings helped me throughout. I would also dedicate this work to my brother Ali Hussain Warsi and my sister Alisha Warsi for their moral support and prayers. Lastly, I would also like to dedicate this work to my special friend Harrum Noor for her moral and emotional support during the final phases of my research work.

Table of Contents

List of Figures

List of Tables

Chapter 1

Introduction

1.1 Digital Radiology

In 1895, William Rontgen accidentally discovered X-rays and paved the path over the next century for a new imaging industry with application pertaining to clinical diagnostics, protein crystallography and non-destructive testing [5, 6, 7]. Radiography refers to an imaging methodology where an X-ray source emits X-rays that are propagated through a patient and then read by an X-ray detector.The X-ray is attenuated by the patient due to difference in the material composition of the object that causes a change in the intensity of the X-ray photons detected by the X-ray detector which can then be used to plot the bright and dark regions and form a two-dimensional contrast image.

Radiography is the initial step for diagnosis of different clinical situations. It is relatively low cost, easily available and non-invasive albeit exposes patients to minimal X-ray radiation dose. Originally dominated by film, today's radiography is dominated by digital X-ray detectors and systems due to proliferation of digital technology conventional radiography suffered from poor workflow and higher patient dose leading to its eventual replacement by Digital radiography (DR). The figure 1.1 shows a typical system for digital X-ray imaging system.

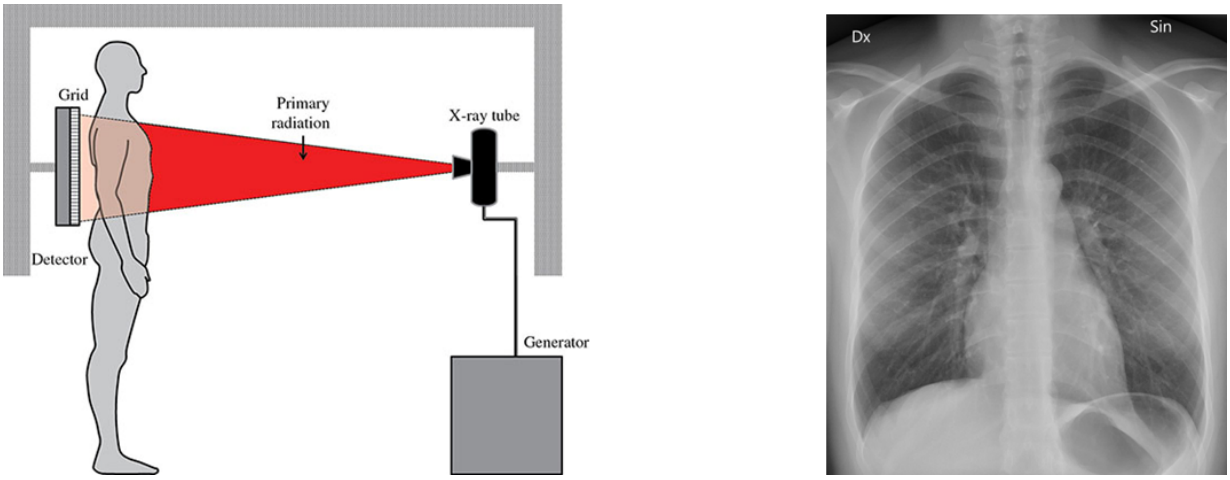

Figure 1.1: System diagram of a typical digital x-ray imager. Source [Wikipedia and Radiology Key]

1.2 Direct and Indirect Conversion

The fundamental working for a digital X-ray detector involves two important steps, firstly the conversion of X-ray photons into electrical charges and secondly the detection of analog to digital electronic read-out circuit. X-ray detectors can be classified based on the charge conversion methodology employed through the X-ray absorption layer. The two different types of conversion techniques used to date are direct and indirect conversion. For direct conversion, a photo-conductive semiconductor is used to absorb the X-ray photons and convert them directly into electrical charges which are then collected using an applied electric field [8]. In contrast, the indirect conversion method converts X-ray photons to visible photons using a scintillator layer and then converts the visible photons to electrical charges using an additional photo-detector element at each pixel. In either of the methods used the charge produced is collected using a solid-state pixel level readout circuit in technologies such as amorphous silicon (a-Si) TFT or complementary metal oxide semiconductor (CMOS). Figure 1.2, below shows the working fundamentals for both direct and indirect conversion methods.

Indirect conversion detectors are adversely affected from the lateral spreading of the op-

tical light that produces a blurred image and degrades the spatial resolution. [9] [10]]. For applications pertaining to high spatial resolution, the majority of available digital x-ray detectors employ indirect detection methodology. For dynamic imaging applications indirect detectors also provide a fast temporal response due to the use of low lag PIN photodiodes and easy coupling to the scintillator material. The spatial resolution limitations associated with optical photon spreading in indirect detection are a limitation for niche applications such as mammography and are resolved by using direct detection X-ray detectors where, a uniform electric field is created by applying a high voltage on the photo-conductor. This field then drives the X-ray photon generated charge towards the collecting electrode to be further processed by the readout circuitry. The lack of light spreading and the application of an electric field using a direct detector allows a higher spatial resolution to be achieved [9]. However, the necessity of a external voltage (typically in mega volts) to produce an electric field is one of the drawbacks for the direct detection method. The material for the photo-conductor plays an important role in the design of the direct detector [8],[11]. Chemical properties such as a high atomic number is essential for complete incident. The energy required to generate an electron hole pair should be low for the detector to have a higher sensitivity. A high dynamic range requires a low amount of dark current and the mobility and life time for carriers should be less than the image readout time or the inter-frame time of the dynamic type detector to be able to collect the photo-induced charges without incurring a residual image.

The commercially available options for the photo-conductor material which meet the properties discussed above comprise of amorphous selenium (A-Se), Cadmium Telluride (CdTe) and Cadmium Zinc (CZT) [12, 13, 14, 15, 16]. The table 1.1 summarizes the material properties of some of the other commercially available photoconductors [17].

1.3 Amorphous Selenium as a Photoconductor

Amorphous selenium (A-Se) was used in photocopying machines as a photo-receptor for 30 years since the mid-1950s until it was replaced by nascent CCD and CMOS optical cameras

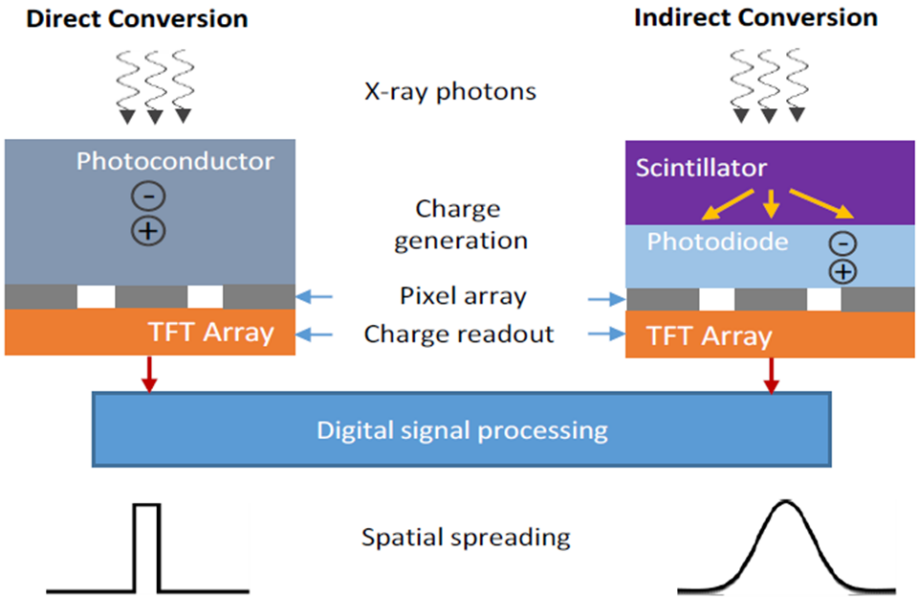

Figure 1.2: Representation of direct and indirect detection techniques of X-ray photons [1]

Table 1.1: A-Se properties fabricated in G2N lab [1] and in literature [3, 4]

Photoconductor	a-Se	CdZnTe	HgI_2	PbI_2
Absorption depth at 30keV(μm)	149	81	91	137
W(eV), τ_h (μs)	50	5	5	5
Resistivity($\Omega.cm$)	$10^{14} - 10^{15}$	10^{11}	4×10^{13}	$10^{11} - 10^{12}$
$\mu_e\tau_e(cm^2/V)$	0.3×10^{-6} - 10^{-5}	2×10^{-4}	$10^{-5} - 10^{-4}$	7×10^{-8}
$\mu_h\tau_h(cm^2/V)$	$10^{-6} - 6 \times 10^{-5}$	3×10^{-6}	10^{-6}	2×10^{-6}
Intrinsic concentration (cm^{-3})	10^{15}	10^{10}	10^{11}	10^{12}
Band gap energy(eV)	1.9-2.3	1.4-2.2	2.1-2.2	2.3-2.4

and became one of the highly used photoconductors in the imaging industry. Selenium exists naturally both in crystalline and amorphous form. Electron mobility is determined mainly by the number of shallow traps which traps and releases the charge carriers multiple times while they travel inside the photo-conductor. Hence, the effective drift mobility is affected by the time a charge carrier remains in the trapped state. The lifetime of charge carriers is determined by the deep electron and hole traps. For amorphous Selenium the conduction mechanism is trap limited transport. For mammography applications, the photoconductor sensitivity is mainly defined by the Schubweg of the charge carriers and limited by deep trap concentration. Schubweg can be explained as the average drift distance by a free charge carrier, it is given by $\mu\tau E$, where μ and τ are the mobility and the lifetime of the carrier, respectively, and E is the applied electric field.

Amorphous Selenium having high purity can crystallize with time and its electrical properties can be effected [18, 19]. The Selenium used for flat panel detectors is referred to as stabilized amorphous Selenium. S.Kasap [3] in his work showed that the rate of crystallization for amorphous Selenium can be controlled by alloying A-Se with small amount of Arsenic (As). However, the setback of using this process includes the reduction in hole lifetime and introducing more deep hole trap states. Chlorine (Cl) can be added to compensate for the adverse effect. This allows to optimize the thermal stability and carrier transport properties of stabilized amorphous selenium by [20].

A-Se can be easily vacuum coated over a large area of up to a thickness of 1000 μm with uniformity over x-ray detectors. It requires the heating of the substrate to be around 65-70

degrees Celsius to thermally evaporate A-Se on to the detector, this process step doesn't adversely effect the performance of the readout circuit like a-Si TFT active matrix array [21] and is thus a favourable material for fabricating x-ray detectors[3]. The thick layer of amorphous selenium has a very good absorption of X-ray photons within the medical imaging energy range despite Selenium having a lower atomic number. The dark current for A-Se is low due to it's high electrical resistivity ($\approx 10^{14}$ Ω.cm) even with a high electric field applied [22]. A-Se is also a good photoconductor for mammography [22] since the K-edge for a-Se lies at 12.7 KeV. The re-absorption of K fluorescent photons having high energies mostly occur at a distance from the initial position of the actual photon interaction, this results in the degradation of the spatial resolution in the detectors. This issue however, can be controlled by the application of a high electric field.

Despite mentioning all the positive aspects, the charge transport properties for amorphous Selenium are not the best to be able to achieve a high charge collection efficiency, specifically under a lower electric field and a thick layer the photoconductor [23, 24, 25, 26, 27]. The charge collection efficiency for holes is sufficient better when compared to electrons for a-Se this is because of the high density of energy-distributed defect states which results in the trapping of the carriers drifting within the a-Se layer[28, 29].

1.4 X-ray Interactions in Photoconductors

Medical X-ray imaging typically uses X-rays in the hard X-ray energy range of 10-120 keV, which can interact with matter through a variety of mechanisms including scattering, penetration, and absorption. The primary types of interactions that occur in this energy range are Rayleigh scattering, Compton scattering, and the photoelectric effect.The photoelectric effect and Compton scattering are mechanisms through which X-ray photons are absorbed and scattered, resulting in attenuation of the X-ray beam and a reduction in its intensity.In contrast, Rayleigh scattering is an elastic, or coherent, scattering of X-ray photons by atomic electrons that does not involve an exchange of energy between the X-ray photons and the photoconductor. As a result, this interaction does not cause a local de-

position of energy in the medium, and the energies of the incoming and scattered photons remain identical.

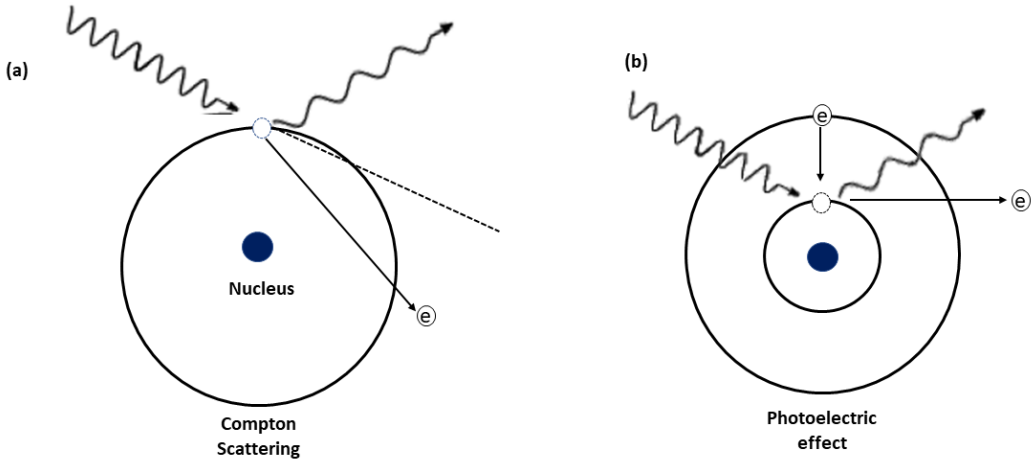

Figure 1.3: (a) Illustration showing Compton scattering with an incident X-ray interacting with an outer-shell electron, producing an electron with kinetic energy E", an ionized atom and a scattered X-ray photon with energy E', b) Illustration for the photoelectric effect showing, showing an incident X-ray being completely absorbed by an electron, which allows the electron to escape the atom resulting in ionization. The electrons from the outer shell than fill in the vacancy in the inner shell producing a fluorescent X-ray

Both the photoelectric effect and Compton scattering contribute to the absorption of energy in the photoconductor. Compton scattering is an inelastic scattering process that occurs when the energy of the incoming photon is higher than the binding energy of the atomic electron. During this interaction, a quasi-free electron is produced with some kinetic energy (E"), along with an ionized atom and a scattered X-ray photon with reduced energy (E') due to the energy imparted to the electron.Figure 1.3(a) above depicts the Compton scattering process, which is characterized by a random scattering angle that

influences the amount of imparted energy. Notably, the Compton scattering cross-section is nearly independent of both the energy of the incident photon (E) and the atomic number of the photoconductor (Z). In contrast, the cross-section for photoelectric interaction is proportional to Z^3/E^3 [30].

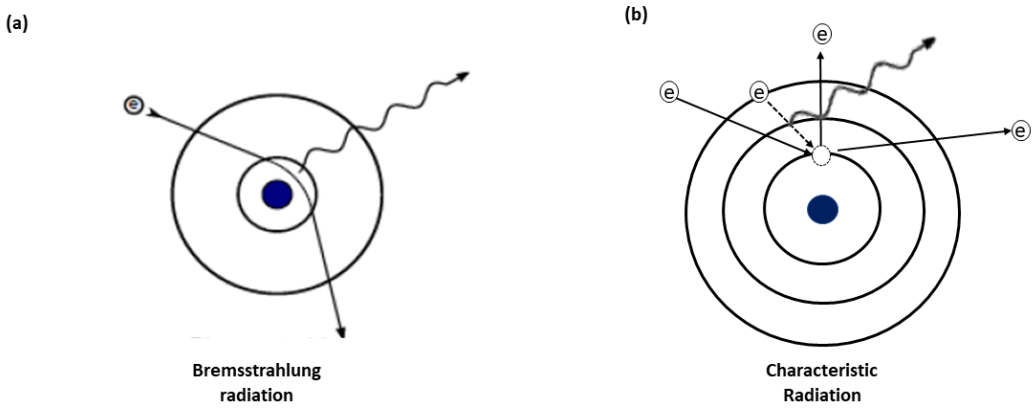

Figure 1.4: (a) Illustration showing Bremsstrahlung radiation being produced because of deceleration in energetic electrons due to the electric field of the nuclei (b)Illustration depicting characteristic radiation showing a cascade of electrons transitioning due to an inner electron escaping from an inner core shell and creating a vacancy in the parent atom.

Figure 1.3(b) above illustrates the interaction through the photoelectric effect, which results in the total transfer of energy from the X-ray photon to the photoconductor. In this process, a portion of the energy is used to overcome the binding energy of the electron, while the remaining energy is converted into the kinetic energy of the free electron. Photoconductors with high atomic numbers, such as a-Se (Z=34), attenuate hard X-ray energies primarily through photoelectric interaction. This interaction occurs when the energy of the incident photon is sufficient to eject an electron from a bound shell. If the photon energy

is insufficient to eject an electron from the innermost K-shell, an electron from an outer shell (such as the L or M shells) can be ejected instead, initiating a cascade electron transition process that produces characteristic X-rays (e.g. K-fluorescent, L-fluorescent, etc.). These characteristic X-rays can be absorbed by the same or neighboring pixels, depending on their energy, and can also cause incomplete energy transfer, ultimately degrading detector sensitivity [31]. The energy of the characteristic X-ray is an intrinsic property of the photoconductor and lower characteristic X-ray energies are desirable to maintain adequate spatial resolution and sensitivity [32].For instance, in a-Se, the energy of the K-fluorescent photon is 12.66 keV, which can be absorbed in a practical photoconductor thickness without significantly degrading spatial resolution and sensitivity. When an electron is ejected from a bound shell, it creates ionization along its trajectory and generates electron-hole pairs. As the ejected electron travels, it interacts with the nucleus and orbits of the atoms through Coulomb interaction, losing energy in the process. This energy loss is converted to bremsstrahlung radiation, as illustrated in Fig 1.4, along with the formation of characteristic X-rays.

1.5 Sensitivity

The sensitivity of a photoconductor, which is used to detect X-ray photons, is determined by the efficiency at which it converts incident X-ray photons into an electrical charge that is stored on the pixel's capacitance. Generally, the higher the sensitivity of the detector, the lower the amount of radiation that needs to be used in order to produce an X-ray image of adequate quality. The sensitivity of an X-ray imaging detector can be quantified by measuring the amount of electrical charge that is collected per unit area for each unit of incident radiation exposure. The sensitivity of an X-ray detector is commonly represented by the formula:

$$S = \frac{Q}{AX} \tag{1.1}$$

where Q is the collected charge in Coulombs (C), A is the area of the detector in

centimeter square (cm^2) and X is the radiation exposure in Roentgens (R). This unit of sensitivity is $C/(cm^2.R)$.

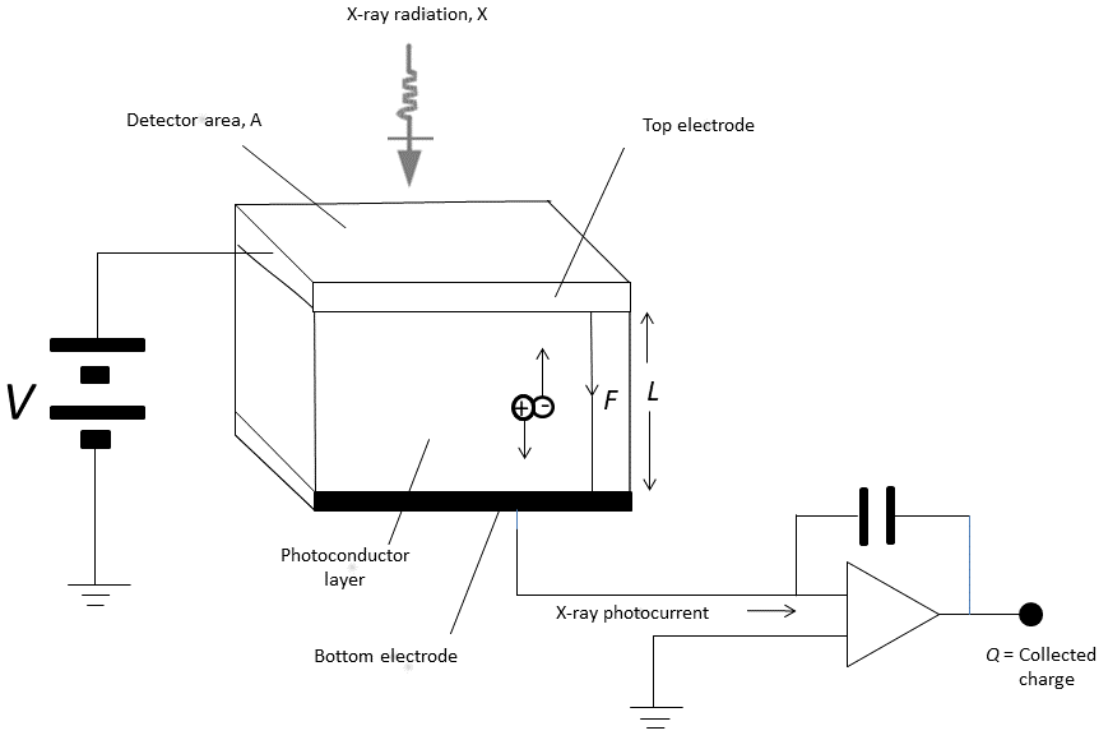

Figure 1.5: Diagram depicting the simple working of a x-ray detector

The sensitivity of an X-ray detector is dependent on three key factors: 1) the ability of the photoconductor to absorb X-ray photons, 2) the conversion of these absorbed photons into free electron-hole pairs (which requires a specific amount of energy known as the ionization energy), and 3) the fraction of the resulting electrical charge that is collected. The fraction of X-ray photons that are attenuated within the photoconductor is described by the term "quantum efficiency" (η), which is largely determined by the linear attenuation

coefficient $\alpha(e)$ and the thickness (L) of the photoconductor that the X-ray photons pass through. The quantum efficiency of a photoconductor is represented by the formula:

$$\eta(E) = 1 - e^{-\alpha(E)L} \tag{1.2}$$

$\eta(E)$ here has a range from 0-1. The photo-conductor thickness should be higher than the attenuation depth, or mathematically $L >> \alpha^{-}1$, to improve the quantum efficiency. The linear attenuation ,α, is linked to the density and the atomic number of the photo-conductor, energy of the incident x-ray photons. Similarly, a higher atomic number is preferable for higher x-ray attenuation. An example of this would be the average energy of X-rays utilized in mammography being 20 kilo-electronvolts, requiring an a-Se layer thickness of around 200 micrometers to effectively absorb most X-ray photons. On the other hand, using a-Se for chest radiography examinations requires the layer thickness to be close to 2000 micrometers with an average energy of 60 kilo-electron-volts.

1.6 Dark Current

Dark current can be defined as an undesired electrical current generated inside the photo-conductor due to the necessary application of electrical potential on the detector electrodes. The flat panel detectors work by integrating the charge collected from the photoconductor, the dark current adds upto the noise component of the system while reducing the dynamic range of the detector. Efforts have been made to characterize and understand the dark current signals in amorphous selenium based detectors [33, 34, 35, 36, 37]. Another factor that normally contributes to the dark current is thermal generation of the charge carriers inside the bulk of the photoconductor. However, for amorphous selenium the thermally generated charge carriers are insignificant because of the large mobility gap (2.2 eV) that exists in the photoconductor material. Therefore the most prominent factor contributing to dark current inside amorphous Selenium detectors is the injection of charge carriers through the detector electrodes [38]. Regardless of the ample amount of research on the presence dark current in flat panel detectors, the phenomenon still remains to be completely understood.

The dark current for amorphous selenium photoconductors can be suppressed by using a blocking layer between electrodes and the photoconductor material. A good blocking layer material will have a high trap density and low mobility for either holes or electron and will allow the passage for collection for the other type of charge carrier. Research shows that the prominent source contributing to the dark current is the hole injection occuring through the positively charged electrodes. Research shows [39, 40, 29] that polyimide (PI) layer can used to limit the hole injection happening through the biased electrodes of the device and can be used to prevent the crystallization and photo-induced darkening inside the detector.[41, 42, 43]

1.7 Photocurrent Lag and Ghosting in Selenium

For large area direct conversion x-ray detectors the photoconductor material may either be in poly-crystalline or amorphous form. The charge carrier transportation is different due to the trapping effect for electrons and holes. This results in schubweg-limited charge transport and in turn decreases charge collection efficiency [44]. Chota Et.al reports the presence of memory artifacts in x-ray images due to spill over because of the remaining signal from earlier exposures into subsequent image frames [45]. These memory effects than reduce gradually and account for the interference in carrier transport because of the trapping effect inside the bulk of the photoconductor material and degrades the detectors temporal response.

The memory effects occurr due to the presence of two major factors. Firstly, a continuous photocurrent lag which is linked to a higher dark current after the detector is exposed to x-rays. Secondly, ghosting which is defined as the change in the sensitivity of the detector due to past exposures. Ghosting can be studied in successive x-ray exposures [12, 46]. Previously, Time-of-flight technique has been used to measure the transient photoconductivity to study the spatial distribution of radiation-induced trapped space charges. The results from the study showed that a net negative trap space charge is formed after exposing the detector to x-rays for a positively biased amorphous selenium (a-Se) photoconductive film. This in-turn causes an increment in the electric field at the top electrode

[47]. It is important to note that decrement in sensitivity is also due to the recombination of holes and trapped electrons [48].

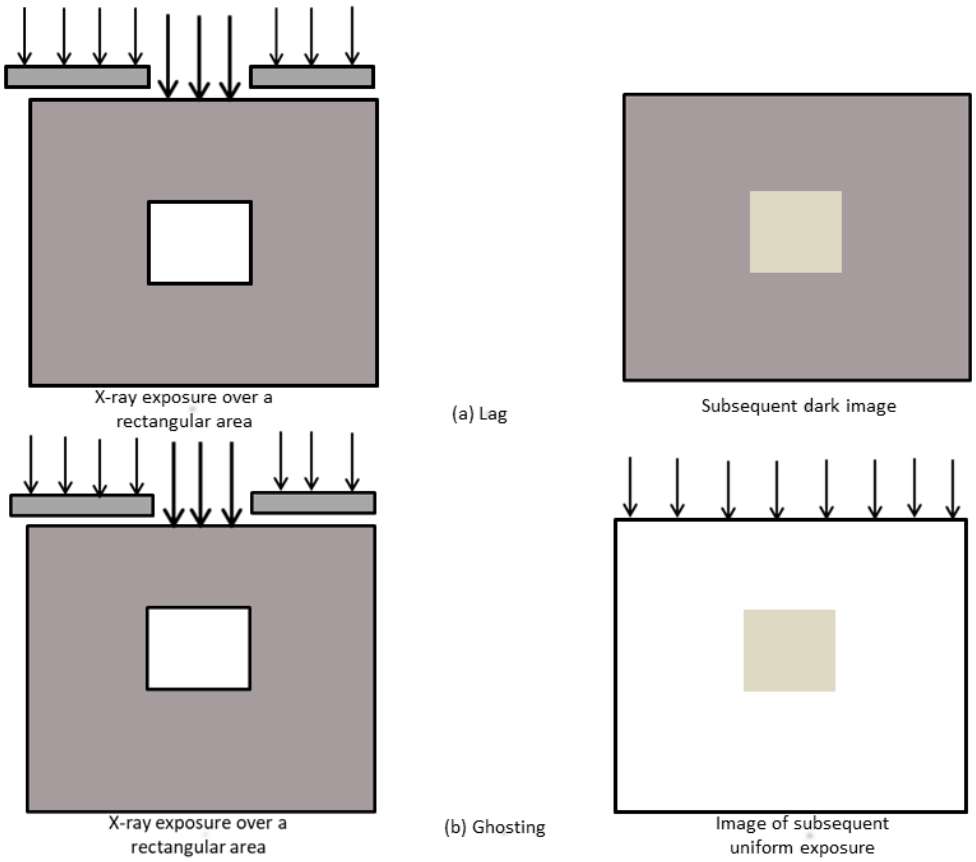

Figure 1.6: An Illustration showing the effects of lag and ghosting on x-ray images.

The temporal response of a detector can be characterized using both lag and ghosting components of the detector. Lag can cause an increase in the pixel value in the region where the pixel had been exposed earlier. Whereas, ghosting would result in the reduction of the pixel value and can be measured in the subsequent x-ray images. The time it takes for a detector to respond to an image is crucial for high-speed imaging techniques such as fluoroscopy. Currently, the best performing commercial flat panel detectors (FPDs) use a-Se technology. However, these detectors are not suitable for high-speed imaging as the

increased lag negatively impacts the temporal response. This issue of image lag is prevalent in most direct conversion photoconductors, such as HgI2 and PbO, and as a result, these materials are not widely used in commercial FPDs. However, it has been found that while ghosting can be an issue with high doses, it is not a significant problem in typical clinical doses. Examples of lag and ghosting can be shown through x-ray images taken over a rectangular area. The figure below shows (a) The image immediately after x-ray exposure will appear dark and display an increase in pixel values in areas that have been previously exposed, which is lag. (b) When a new image is taken with a uniform exposure, a faint shadow of the previous image may appear, which is ghosting, it is caused by a decrease in pixel sensitivity in previously exposed areas and can only be seen in subsequent x-ray images.

1.8 Motivation

Majority of the mammography detectors being used today employ energy integration methodology which are limited by the amplifier noise present in the readout circuit. This problem is more persistent in the low x-ray exposure areas and thus require extra radiation to compensate for the signal lost. The other downsides of using the existing direct flat panel detectors (FPDs) for x-ray imaging comes with low dose efficiency. Despite the inherent spatial resolution achieved by using a-Se as a photoconductor the real time imaging applications such as micro-angiogrpaphy suffer from lag in the signal which limits the frame rate of the x-ray images produced.

A slower frame rate is linked to lag which in turn occurs due to the temporary rise in dark conductivity. Due to a high lag the image frames produced carry spill over signal stored from the previous exposure. Photocurrent lag is one of the important factors which contributes to lower image quality for a-Se x-ray detectors due to extensive charge trapping in the amorphous selenium layer. A-Se has the potential to be a suitable option for photon counting, owing to its high sensitivity, capacity for room temperature operation, and high bandgap of 2.2 eV, which allows for the lowest dark current of any commercially available

photoconductor. Moreover, A-Se can be applied over a wide area as a thick film, thereby lowering manufacturing costs. However, A-Se is not considered a viable photoconductor for dynamic radiation imaging applications because of its low temporal resolution. Although holes can be collected efficiently in A-Se, electrons are typically collected less efficiently, with a mobility lifetime product approximately one order of magnitude lower than that of holes. Since photon interaction occurs randomly in the detector volume, the electrons generated must drift across varying distances to reach the collecting electrode. As a result, signal rise time varies due to electrons with slower mobility, creating depth-dependent noise. Therefore, this work focuses on designing and fabricating an x-ray detector to overcome the challenges mentioned above.

1.9 Thesis Objective and Organization

The objective of this works includes the design, fabrication and testing for amorphous selenium based x-ray detector with metal frisch grid like structure that can help improve the lag commonly occurring in conventional x-ray detectors. It explores the possibilities of improving the current lag using the unipolar charge sensing detector for direct conversion methdology. This work proposes the use of metal grid electrodes inside the x-ray detector to help improve the current lag in the signal collected. The metal grid can promote selective sensing of holes, fast charge carriers, inside the detector. This helps improve the charge collection efficiency as the induced charge depends on the mobility of fast charge carriers travelling over longer distance inside the detector. This insensitivity to the collection of slow charge carriers which are electrons can help further improve the lag in the detector. Thus, this could help achieve a higher x-ray sensitivity.The scope of this thesis includes how the detector design including theoretical discussion and simulation results. The fabrication steps involved in the development of the detector. Lastly, the detector was tested for dark current and photocurrent measurements. The thesis is organized with chapter 1 starting with the introduction to digital radiology. It further discusses the classification of x-ray detectors with regards direct and indirect conversion methodologies. Moving on, it discusses the importance and effectiveness of using amorphous selenium as a photo-conductor. It

further explains how it plays an essential role in current x-ray detectors. The chapter ends discussing the motivation behind the work and the objective and thesis organization. The 2nd chapter of the thesis discusses and explains the metrics of the detectors performance like sensitivity, dark current, photocurrent lag, ghosting. It further explains the induced signal analysis and the Shockley Ramo-thoerem in conjunction with the weighting potential to explain how a grid structure can help improve the photocurrent lag issues. Moreover, it discusses the design of the unipolar charge sensing structure and it's simulations to show it can be effective compared to the existing conventional detectors. It presents the charge collection efficiency analysis and simulations including the pulse height spectroscopy and energy resolution results for the designed detector. Chapter 3 follows up with the details of the fabrication and characterization of the unipolar charge sensing detector. It shows the photomask design and shares the specification for the fabrication process of the device. The fabrication process details are discussed beginning with wafer cleaning, dc metal sputtering, photolithography, spin coating, metal wet etching and reactive ion etching. The chapter finally shares the experimental results for the unipolar charge sensing detector and the conventional detector. Finally chapter 4 discusses the conclusions and the future work for the work presented in this thesis.

Chapter 2

Design and Modeling of an Amorphous Selenium Unipolar Charge Sensing X-ray Detector

2.1 Introduction

Energy integration systems are limited in performance and sensitivity due to ineffective noise rejection capabilities [49]. This results in a higher detector noise leading to low signal-to-noise ratio and poor dose efficiency, which is counteracted by introducing a higher radiation dose [50]. Photon-counting is an effective approach which allow efficient suppressing or eliminating the electronic related to the detector. Photon-counting also allows energy weighting which enhances the signal-to-noise ratio in regions having lower contrast for eg: soft tissue [51, 52, 53, 54]. The existing photon counting detectors use cadmium telluride (CdTe) and silicon (Si) as a photo-conductor for breast screening [55, 56, 57, 58]. However, both of the aforementioned materials are not applicable for large area imaging due to the fabrication constraints. Moreover, Silicon has limitations for high photon energy imaging applications due to it's low atomic number. While, Cadmium Telluride has itself has low fabrication yield and inefficient charge transport problems [59, 60].

Amorphous Selenium (a-Se) can overcome these issues linking to photon counting detectors for mammography and tomosynthesis[61]. Amorphous Selenium appears to be a viable solution as it allows cost-effective and effective coupling to large readout interfaces and it provides a high intrinsic spatial resolution and detection efficiency for the beast screening energy range applications with a low k-edge energy at 12.6 KeV in comparison to other photo-conductors. Additionally, amorphous Selenium detectors are easily operational at room temperatures due to their wider band-gap i.e. 2.2 eV [62, 63]. Therefore, Amorphous Selenium based on previous studies fulfills all the characteristics that prove beneficial for photon counting radiation detectors.

Amorphous Selenium despite having the benefits mentioned above, still has some challenges that remain to be addressed to design an improved and efficient photon counting system. The high ionization energy W± and the electron trapping [64, 65]. The charge collection time for every electron-hole pair varies, depending on the photon-interaction depth for every X-ray photon as the a certain portion of the induced signal is dependent on the electrons. Moreover, electron trapping slow electron transport is a major challenge while designing photon counters with amorphous Selenium. Furthermore, electron trapping can occur before the electron reaches the collecting electrode, which largely reduces the charge collection efficiency.

Since the intrinsic resolution is limited by the number of electron hole pairs for a specific photon energy we can conclude the high ionization energy of amorphous Selenium is also a cause for the reduced energy resolution. Recent studies show that this challenge can be tackled by operating the A-Se detector at a very high electric field around (90 V/um). [40, 66, 67].

2.2 Induced Signal Analysis

In doped semiconductors and ionic materials the current on the collecting electrode is zero until a drift charge travels to the respective collecting electrode [68]. This is because of the fact that charge neutrality is maintained at all points in these materials as the photo-

generated charge is covered by the compensating charge. But for high resistivity photo-conductors, since there is no charge neutrality as there is no reservoir for compensating the charges in the time scale concerning the drift charge reaching the collecting electrode. The characteristic relaxation time for any medium can be calculated by $\tau = \epsilon.\rho$ where ρ is the resistivity for the medium and ϵ is the dielectric constant of the material, which is given as $\epsilon = \epsilon_0\epsilon$. The relaxation time for selenium is approximately 1 minute when calculated with the values for, $\rho = 10^{14}$ cm and $\epsilon = 6.7$. Typically, the transit times for carriers lie between a few ten micro-seconds, henceforth a relaxation time of one minute is too long. This however proves that the photo-current that will be collected from the photo-generated carrier is occurring completely because of induction.

The induced charge current for a detector having a single continuous electrode like in the figure below can be calculated using the conversion of energy argument [69, 70]. The total power required to move a charge package, q, at a velocity v in the direction of the electric field, E, is given by

$$P = q.E.V \tag{2.1}$$

Assuming a constant voltage power supply providing an equal voltage throughout the photo-conductor thickness, L. We know that power is given by the equation:

$$P = I.V \tag{2.2}$$

Where I is the current. I can now be defined as;

$$i = q.V/L \tag{2.3}$$

The charge package can be divided into holes $eN_h(t)$, and electrons eN_e(t), of which both are collected by different electrodes. The densities for both the charges can be changed due to trapping and recombination. Hence the current for a single-continuous pixel electrode can be calculated through the equation:

$$i(t) = e(N_e(t)v_e + N_h(t)v_h)/L \tag{2.4}$$

Considering the collected charge is fed to an active integrator circuit such that the integration time is long enough to allow the charge carriers to be able to travel to the collection electrode inside the detector. Hence, the net charge as a function of photon interaction depth can be represented as:

$$Q(zi) = (eN_e\lambda_e/L)[1 - exp(-z_i/\lambda_e)] + (eN_h\lambda_h/L)[1 - exp(-L - z_i/\lambda_h)] \tag{2.5}$$

where z_i defines the photon interaction depth, L is the thickness of the photoconductor, $eN_h(t)$ and $eN_e(t)$ are hole and electron charge packages. It is to be noted that λ_e, λ_h are the electron and diffusion lengths . Since the pixelated electrodes shows the total current collected by the detector instead of the current collected by each pixel, the energy conservation argument isn't applicable for this case. The electric field, E,(normal component over the surface of pixel electrode S) for each charge carrier trajectory for the pixelated detector can be calculated to further find the total time-dependent charge, Q. This charge which occurs for every electron-hole pair motion can be represented as:

$$Q = \int \epsilon E.ds \tag{2.6}$$

However, this calculation would be very tedious and time consuming to do, realizing the vast number of electric field components that would need to be computed for each point of the charge trajectory and the huge number of electron-hole pairs produced for every incident photon on the detector.

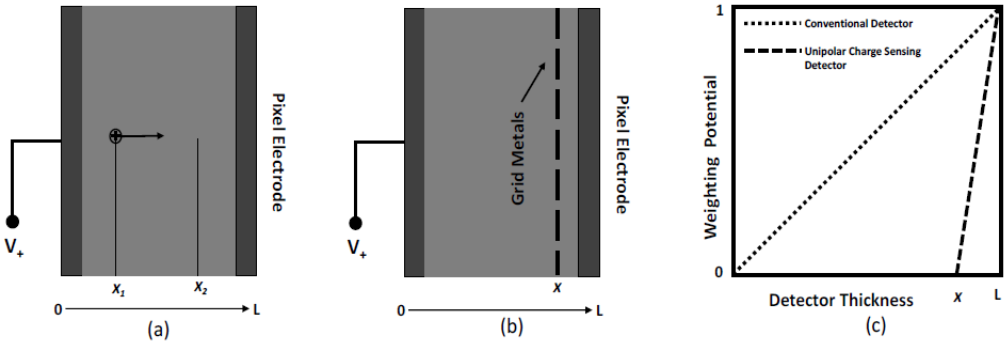

Figure 2.1: (a) Cross sectional view of conventional x-ray detector, (b) cross sectional view of a x-ray detector with internal grid, (c) Weighting potential plots for conventional and unipolar detector [1]

2.3 The Shockley-Ramo Theorem and Weighting Potential

The Shockley-Ramo theorem was published to explain the working inside the vacuum-tubes where normally no space-charge existed, however later on the theorem started being used to explain charges inside semi-conductors with a space charge [71, 72]. It allows to calculate the induced charge on pixelated electrodes in a much quicker and easier manner [71, 72]. The theorem calculates the induced charge within a detector by including the shape and dimensions of the detector and the pixel electrode , weighting potential and the material properties.

The weighting potential can be explained as follows: consider a pixel electrode, i, provided with a unit potential with all other pixel electrodes grounded assuming there is no-space charge inside the detector. The electrostatic potential produced in these conditions is referred to as the weighting potential for a detector. The weighting potential, ϕi, is a dimensionless quantity can be computed using the Laplace equation (eq 2.7) using a finite element analysis software like COMSOL or Xenos by setting the voltage levels for pixel electrode to unit volt. The top and the remaining electrodes are then set to null.

$$\Delta^2\phi = 0 \tag{2.7}$$

Now, we can show the induced charge, Q_i and the current I_i which result due to the motion of the point charge q on the pixel electrode on the pixel electrode i as :

$$Q_i = -q\phi_i(x) \tag{2.8}$$

$$I_i = qv.E_i(x) \tag{2.9}$$

where v is defined as the instantaneous velocity of the moving charge, q and $E_i(x)$ is the conceptual weighting field whose SI unit is m^{-1}.

Considering the charge, q in the figure 2.1(a) moves from position x1 to x2, the induced charge as a result of this movement on the pixel electrode i can be shown as:

$$Q_i = q[Q_i(x_2) - Qi(x_1) \tag{2.10}$$

Which is simplified to:

$$Q_i = [q(x_2) - (x_1)]/L \tag{2.11}$$

where L is the thickness of the photoconductor. It is to be noted that for a conventional detector the weighting potential determines to be a linear function of depth starting at zero from the biased electrode and gradually rising to 1 at the pixel electrode, as can be seen from figure 2.31c). The above discussion can be used to analyze a single element detector with a continuous electrode, $E_i(x) = 1/L$ and $i(x) = x/L$; the induced current can be defined as $I_i = qv/L$. To calculate the weighting potential of a charge q at x on a travel path towards the pixel electrode, the induced charge on the pixel electrode can be defined as $q.i(x)$. This also shows that the charge collected from the pixel electrode and sent to the readout circuit due to the motion in the bulk of the detector is same as $q.i(x)$. If charge,

q, is trapped within the bulk, it can be seen through equation 2.11 that only a portion of the photo-induced charge can be collected by the read out electronics. It is also important to note that induced charge on the collecting electrode is defined by the initial and final location for each of the drifting charge carriers regardless of the detector potential and space charge that might be present.

2.4 Unipolar Charge Sensing Structure Design

Amorphous selenium (a-Se) based flat-panel detectors employing direct conversion methodology has provided good results when it comes to X-ray imaging technology pertaining to applications requiring high spatial resolution and quantum efficiency like mammography when in comparison to indirect conversion. [3, 73, 22, 74, 75, 76, 77, 78].

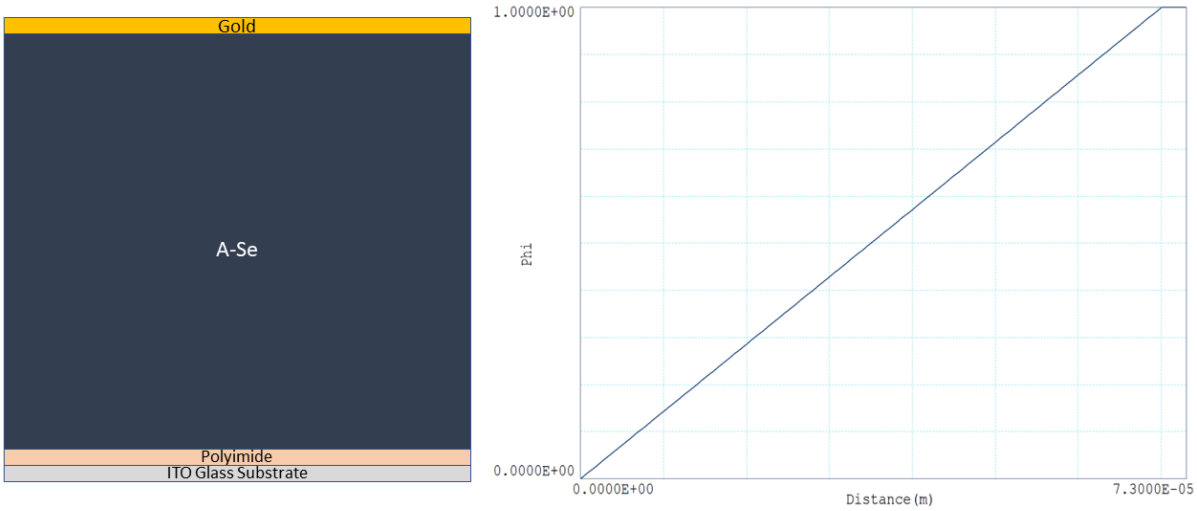

Figure 2.2: Illustration of a conventional X-ray detector with it's weighting potential distribution

However, detectors designed for direct conversion method normally require a high external applied voltage for the formation of a high electric field inside the a-Se layer in-order to separate and collect the generated charges i.e holes from electrons [64, 37]. This large electric field results in the rise to unwanted leakage current in the detector which causes a low signal-to-noise ratio and also leading to constant photocurrent lag [79, 80, 81]. Research has shown that these negative effects can be reduced by an application of an intermediate blocking contact layer between the contact metal and the photoconductor [82, 12]. Recent studies have shown the application of the polyimide (PI) as a blocking layer as a viable solution for limiting hole injections coming in from the positive electrodes in the detector.

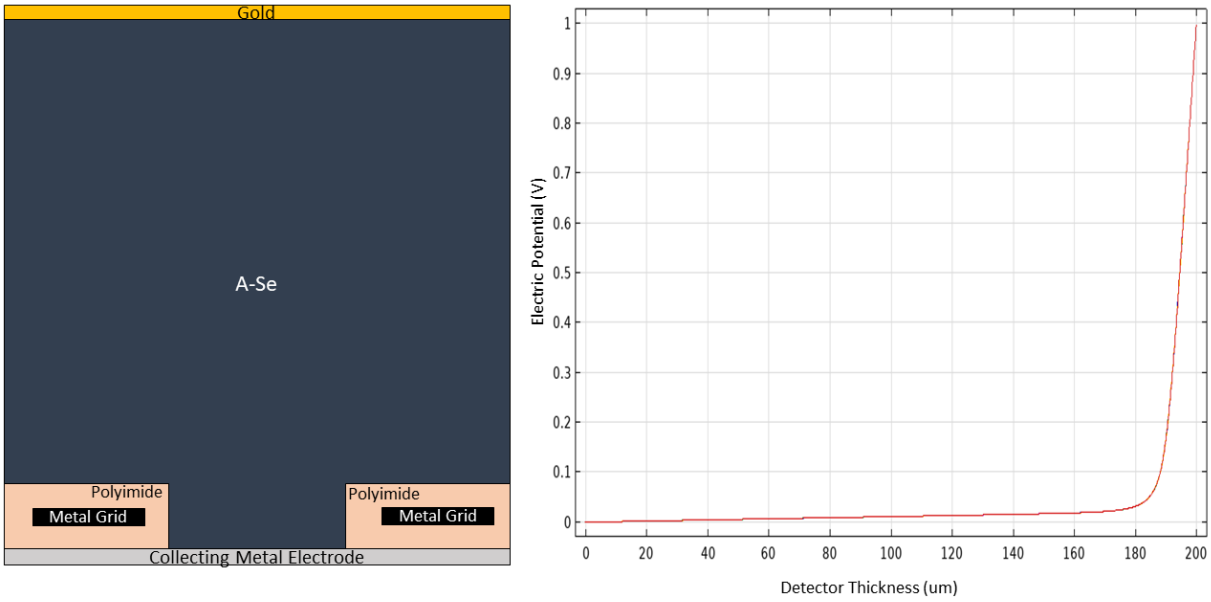

Figure 2.3: Illustration of a unipolar charge sensing detector with its weighting potential distribution

Weighting potential for unipolar charge sensing devices is independent of the depth or thickness of the detector, with either of an internal grid, for eg. Frish grid[27], or with a small pixel effect[83]. This advantage of localized charge sensing can be achieved by producing a strong near-field effect near the pixel electrode. Figure 2.5 shows a fundamental

depiction of a structure for unipolar charge sensing devices. This weighting potential plot shows that the charge induced on the collecting pixel electrode due to the motion of the charge carriers from the top electrode and the grid layer (i.e. far-field) is null. Hence, the charge with a higher mobility are able to pass through the grid layer and contribute to the output signal of the detector. It is important to note the weighting potential plot discussed above is under the assumption of zero charge-trapping inside the bulk of the photo-conductor. The difference in the weighting potential response between the conventional and unipolar sensing device is due to reason that the induced charge on the collecting pixel electrode is directly proportional to the density of the electrostatic flux lines terminating at the corresponding pixel electrode. The flux-line density starting from the top electrode to the pixel electrode is constant throughout the photo-conductor material for the conventional detectors. This is why the weighting potential for conventional detectors is dependent on the detector thickness where it reaches maximum at the collecting pixel. In contrast, the uni-polar charge sensing detector the electric flux lines are distributed evenly inside the bulk but it can be seen from the figure(2.6) below that the grid layer and the collecting electrode region have more denser distribution of the flux lines with each line ending at the collecting electrode.

A unipolar charge sensing device can be designed by the use of an internal metallic grid, Frisch grid, or by producing a small pixel effect [83]. For unipolar charge sensing detectors the weighting potential is independent of the detector's thickness. This is achieved by creating a strong near-field effect near the collecting pixel electrode. The figure below shows the structure for the designed uni-polar charge sensing structure with embedded metal grids, along with the results of the weighting potential.The results for the weighting potential obtained show the majority charge induced on the collecting pixel electrode is due to the near field effect i.e. the higher mobility charge which passes past the metal grids and reaches the near the collecting electrode is collected as output signal for the detector. This also helps us to avoid the slow moving charge carrier, which are electrons when we use amorphous selenium as the photo-conductor, to be collected by the collecting pixel electrode due to the movement of charge carriers from the top electrode to metal grid electrode layer, which is the far-field region. The results produced for weighting potentials

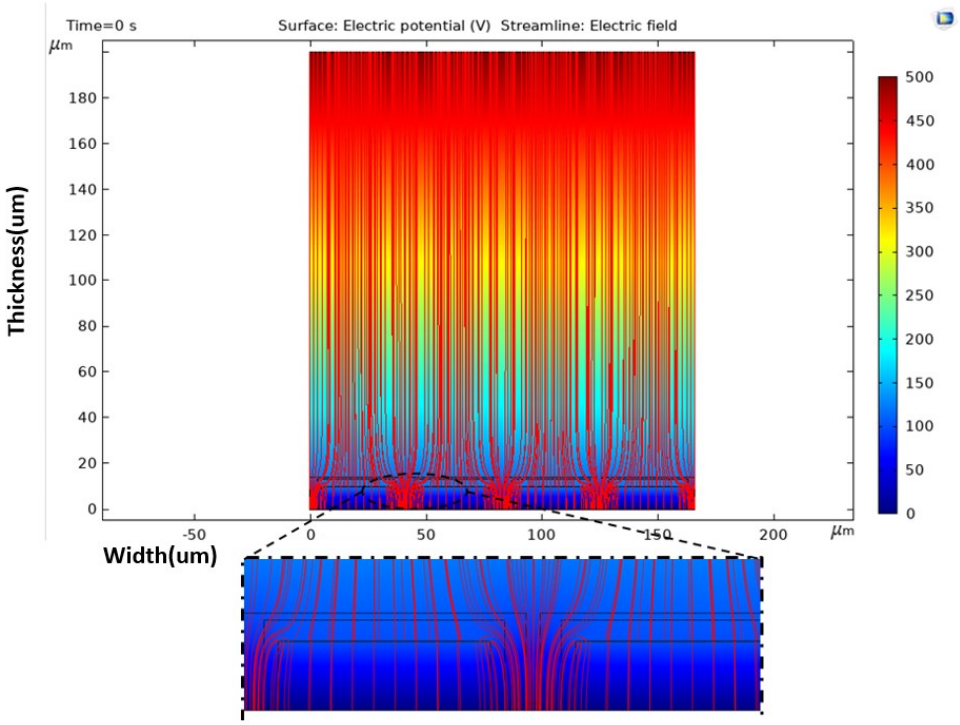

Figure 2.4: Electric field stream line simulation from COMSOL of Unipolar charge sensing detector

ignore the effects produced due to charge-trapping inside the bulk of the photo-conductor. The difference of weighting potential between the conventional and unipolar charge sensing detector can be explained due to the fact that the charge induced or collected on the collecting pixel electrode is directly proportional to the number of flux lines that end up on the corresponding collecting pixel electrode. In the conventional x-ray detectors, the flux lines are constantly proportional to the detector's photoconductor thickness which can be seen as the weighting potential rises constantly with the thickness and reaches 1 when at the collecting pixel electrode. For the unipolar charge sensing detector this is not the case since the flux lines are distributed evenly inside the bulk of the photoconductor and becomes highly concentrated at the region between the metal grid electrodes and the collecting pixel electrode, which is described as the near field region. This helps to increase

the detector's output signal as the dense field lines quickly guides the charge carrier to towards the collecting electrode once it enters the near-field region.

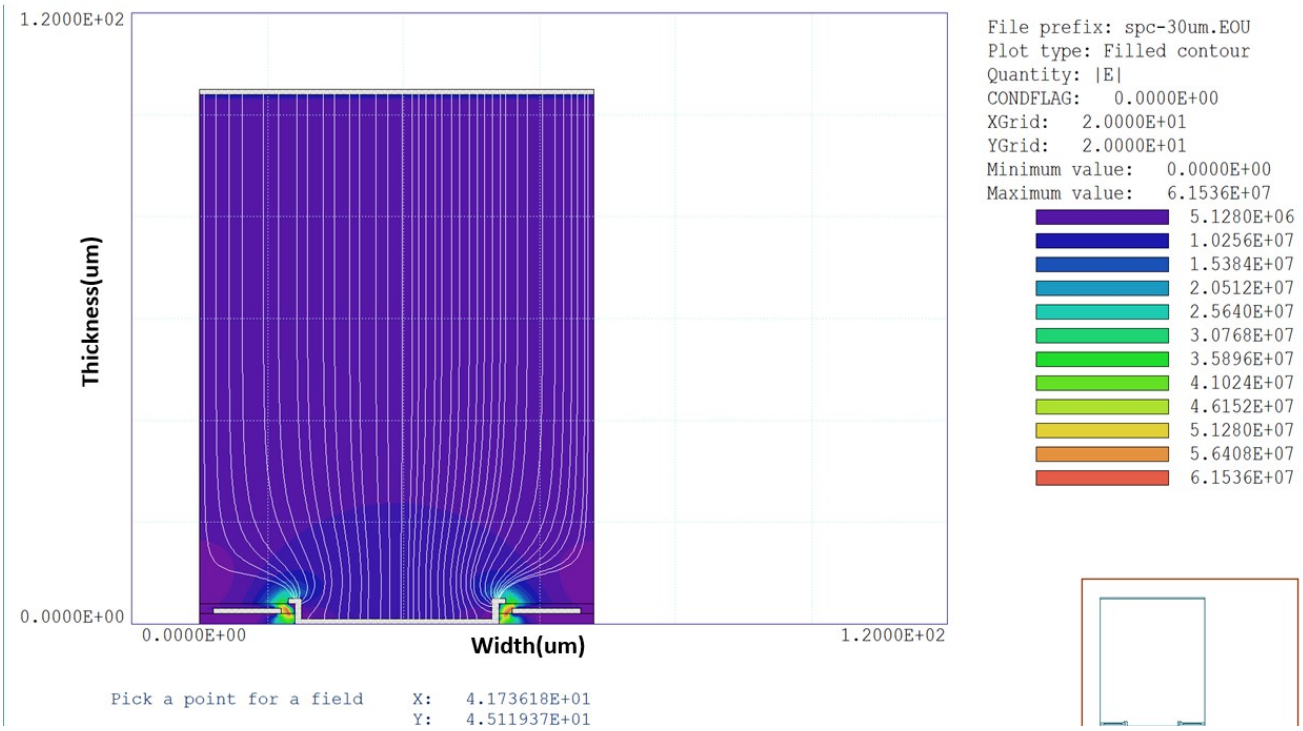

Figure 2.5: Electric field simulation for a 20um pixel size of unipolar charge sensing detector

To finalize the design for the unipolar charge sensing detector the simulation tools (COMSOL and Xenos design suite) were used to test the appropriate voltage biasing for the metal grid and top electrode for efficient charge collection in the device. This allows effective charges with high mobility and lifetime product to be collected which in turn helps maintain a high radiation sensitivity and prevents high charge accumulation on the dielectric layer. The high mobility charge carrier can either be electrons or holes based on the type of photoconductor used in the detector. The biasing thus needs to be defined as positive or negative based on the type of high mobility charge carrier in the device used. This work uses amorphous Selenium as the photoconductor which produces holes as the high mobility charge carrier. Therefore, the top electrode and grid layer are positively

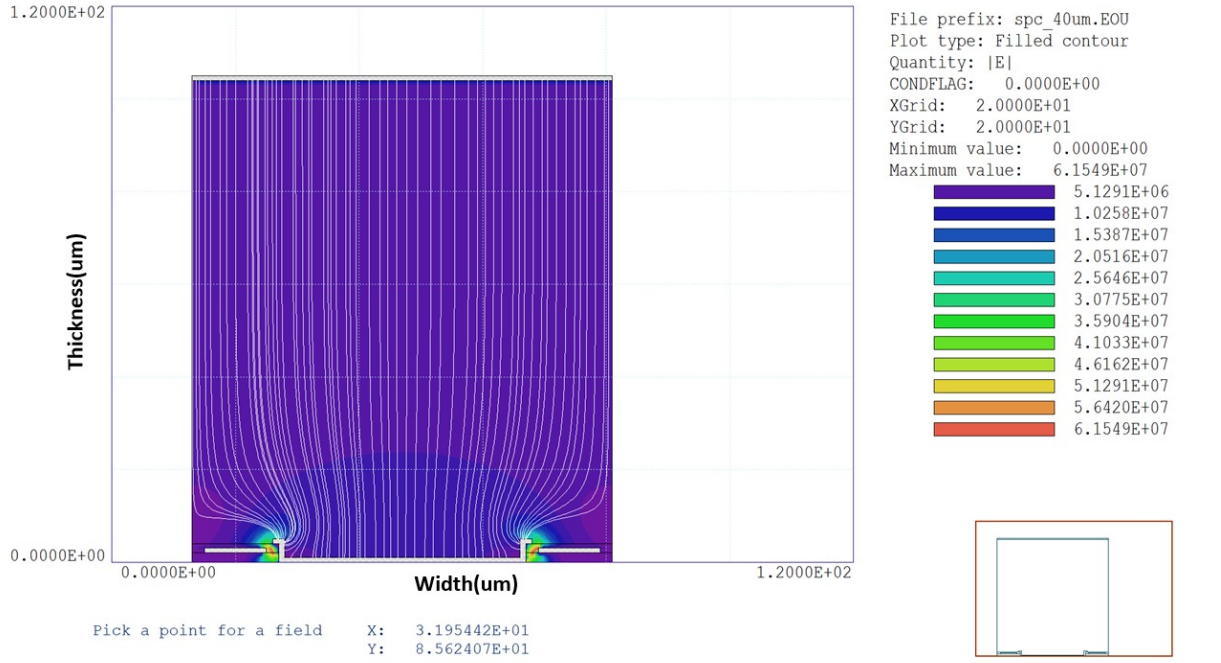

Figure 2.6: Electric field simulation for a 40um pixel size of unipolar charge sensing detector

biased to direct all the photogenerated holes on to the collecting pixel electrode. As per the appropriate configuration a full amplitude of the output signal will be expected at the output of the detector as the photogenerated holes would pass through the near field region and on towards the collecting electrode. Considering the fact that electrons will also be produced once the x-ray photons interact with the photoconductor , even if electrons are trapped between the top electrode and the metal grid electrode region and is not collected at the collecting electrode the output signal will remain unaffected. Different pixel sizes ranging from 30 um to 80 um were designed and simulated on Comsol and Xenos design suite which can be seen in the following figures below.

The figures shows electric field stream lines starting from the top electrode and ending at collecting pixel electrode for different pixel sizes for the unipolar charge sensing detector ranging from 30um to 80um. It was observed that biasing the top electrode and the metal grid layer between 500V to 80V gave the optimum results for each pixel size. The voltage

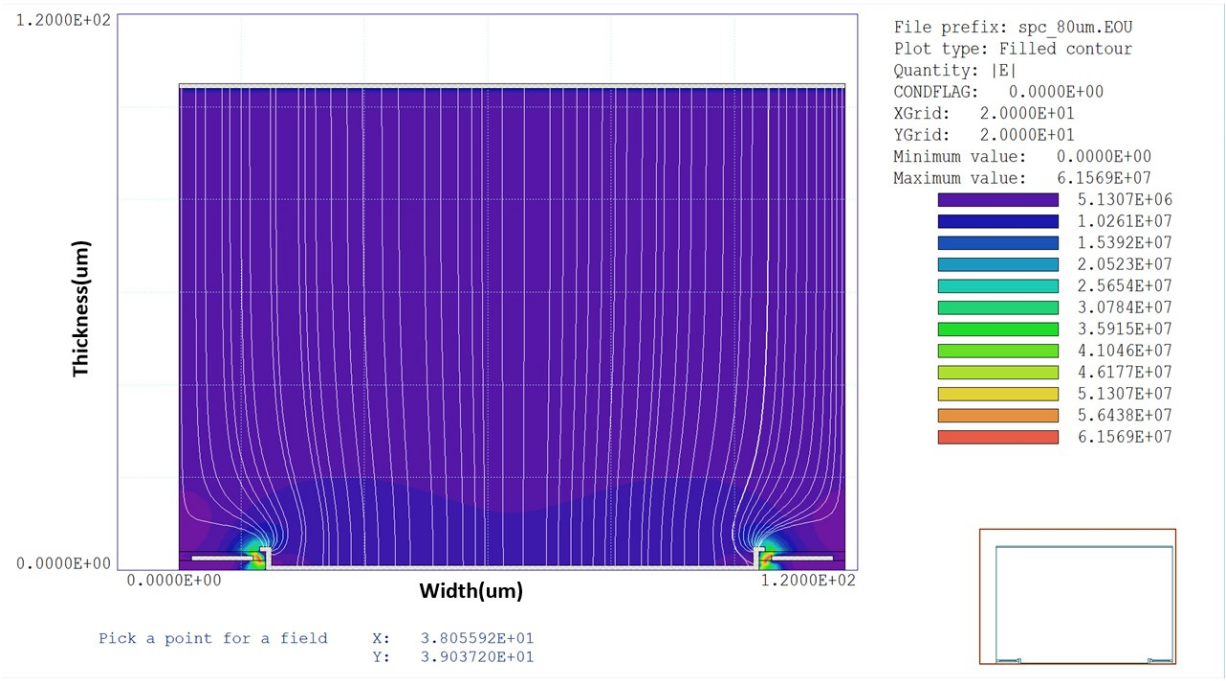

Figure 2.7: Electric field simulation for a 80um pixel size of unipolar charge sensing detector

required to bias the metallic grid layer is dependent on the voltage applied on the top electrode and the thickness of the photoconductor. It was observed the this voltage is inversely proportional to the pixel size. The voltage applied on the metallic grid electrode was always lesser than applied on the top electrode. The chances of a local hot spot formation which eventually leads to an electrical breakdown are less with the small pixel pitches. This is because the metal grid electrode requires a lower voltage with smaller pixel pitches. Setting an electric field ranging from 6V/um to 10V/um resulted in an effective electric field streamline showing all the electric field lines to start from the top electrode and ending up on the collecting pixel electrode which shows that the charge carriers would all end up on the collecting electrode resulting in a high output signal with ideally a charge efficiency approximately at unit.

2.5 Charge Collection Efficiency

A method to describe how uniformly the detector responds to photon interaction at varying depths is by computing the charge induction efficiency. The ideal detector response should produce a signal output that exhibits nearly identical amplitudes across all photon interaction depths, which suggests that the detector is collecting the photogenerated charge with maximum efficiency.The response of the detector is not influenced by the depth of photon interaction. To demonstrate how unipolar charge-sensing can enhance the uniformity of signal output, we performed efficiency calculations for various internal grid pitch ranges, similar to those used in unipolar charge-sensing detectors, and for a conventional a-Se detector. These efficiency calculations also reveal the potential drawbacks of a unipolar charge-sensing device. Our model for efficiency calculation considers the uniform trapping effect on both types of carriers, indicating the impact of a-Se film thickness and electrical properties on detector response. Since the charge trapping process is random, it is best to model it using a probability density function (PDF). Assuming that a photon is absorbed at x1 and that electrons and holes are collected by the top and bottom electrodes, we can express the PDF for electrons and holes trapped at x'1 and x"1, respectively, using the following equations:

$$p_{top}(x_1'|x_1) = \alpha' e^{-\alpha'(x_1 - x_1')} \tag{2.12}$$

$$p_{bottom}(x_1''|x_1) = \beta' e^{-\beta'(x_1'' - x_1)} \tag{2.13}$$

here α' and β' are defined as coefficients of linear attenuation for electrons and holes respectively, and are given as:

$$\alpha' = \frac{1}{\mu_e \tau_e F_1} \tag{2.14}$$

$$\beta' = \frac{1}{\mu_h \tau_h F_1} \tag{2.15}$$

The current induced by the holes and electron on either of the electrodes has the same polarity. Hence, the total charge induced is a summation of both carriers. The charge collected on the bottom electrode because of a moving hole generated at position x1 on the detector can be defined by:

$$Q_{bottom}(x) = \sum_{m=x_1+1}^{N-1} [V_W(x_1) - V_W(m)][e^{-\beta'((m-x_1)} - e^{-\beta'((m+1)-x_1)}] + e^{-\beta'(L_1-x_1)}[V_W(N) - V_W(x_1)] \tag{2.16}$$

For the top electrode, the charge generated as a result of a moving electrode at x1 is given by:

$$Q_{top}(x) = \sum_{m=1}^{x_1-1} [V_W(x_1) - V_W(m)][e^{-\alpha'((x_1-(m+1))} - e^{-\alpha'(x_1-m)}] + e^{-\alpha'(x_1)}[V_W(N) - V_W(x_1)] \tag{2.17}$$

where $\Delta x_1 = L_1/N$ can be described as the uniform step size and the spatial number of divisions are denoted by the letter N. The discrete point $x_1 = x_i \Delta x_1$ where x_i is an integer ranging from 1 to N. We assume the weighting potential (V_w) to be constant within each step. The total collected charge because of an Electron hole pair generate at location x_1 inside the detector can be given by:

$$g_4(x_1) = Q_{grid}(x_1) + Q_{top}(x_1) \tag{2.18}$$

Figure 2.10 displays the outcomes of the computation of charge collection efficiency for 70 micrometer-thick selenium that was operated at 8 volts per micrometer for two distinct a-Se films that possessed different electrical properties. These a-Se film properties, which are summarized in Table 4.1, were used to conduct the aforementioned computation. One of the films was made at G2N University of Waterloo [1], while the other one had poor electrical properties that were obtained from the literature, indicating poor quality of the

Table 2.1: A-Se properties fabricated in G2N lab [1] and in literature [3, 4]

	Fabricated G2N	Reported in Literature
Hole Mobility, μ_h, $(cm^2/V.s)$	0.147	0.13-0.15
Hole Lifetime, τ_h (μs)	120	50-500
Electron mobility, μ_e $(cm^2/V.s)$	0.004	0.002-0.004
Electron Lifetime, τ_e (μs)	200	200-1000

a-Se film. The sample that had poor electrical properties had a low hole-lifetime, therefore, we anticipate that the time response of a unipolar charge-sensing device could be restricted. The purpose of this is to demonstrate the feasible limitations that could be imposed on a unipolar charge-sensing device due to poor hole transport. Conversely, by using a-Se with high electrical quality, we can reveal the intrinsic temporal response limitations of an a-Se-based unipolar charge-sensing device.

Figure 2.10 shows that the highly non-uniform response of a conventional detector with our a-Se layer can be attributed to poor electron transport properties. The charge induction efficiency has a downward curvature on the collecting electrode side, which is a result of electron trapping. The photo-generated electrons at this side must travel a longer distance, but some of them may become trapped due to their shorter Schubweg before reaching the top electrode. However, we observed that the response for the unipolar charge sensing device was uniform, as the detector response solely relied on hole transport, and it improved with a smaller grid pitch. The small curvature on the collecting electrode side is due to photon absorption in the near-field region. Therefore, photo-generated electrons induce a degree of signal on the collecting electrode, but some of them become trapped before reaching the top electrode. However, this is a minor effect on the output signal of the unipolar charge-sensing device because the likelihood of having photon absorption in the near-field region is relatively low due to the small region.In regards to the other device with poor electrical properties, the detector response suffers from even hole-trapping, particularly for events that occur close to the top electrode, as seen in Figure 2.11.

The holes' Schubweg is degraded due to their short hole-lifetime, causing some of the holes to become trapped before being collected by the collecting electrode. This poor

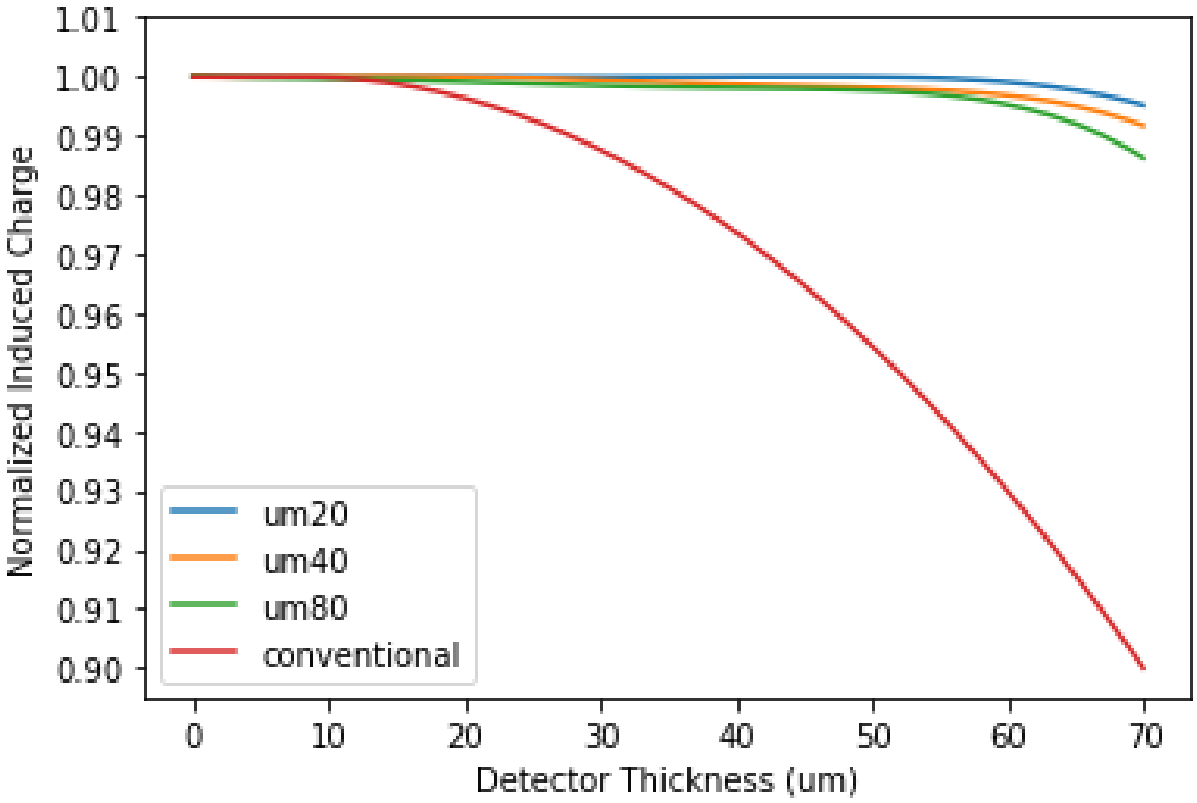

Figure 2.8: Calculated charge induction efficiencies graph with respect to detector thickness for the device created in G2N

hole-lifetime effect extends further into the unipolar charge-sensing device since the charge induction with the unipolar charge-sensing primarily relies on hole transport. As some of the holes become trapped before reaching the collecting electrode, the induced charge signal is lower than what would result if only holes passed entirely through the grid layer and were collected by the collecting electrode.It should be noted that the simulations performed were for our fabricated device, which only has a 70-micrometer-thick a-Se layer.

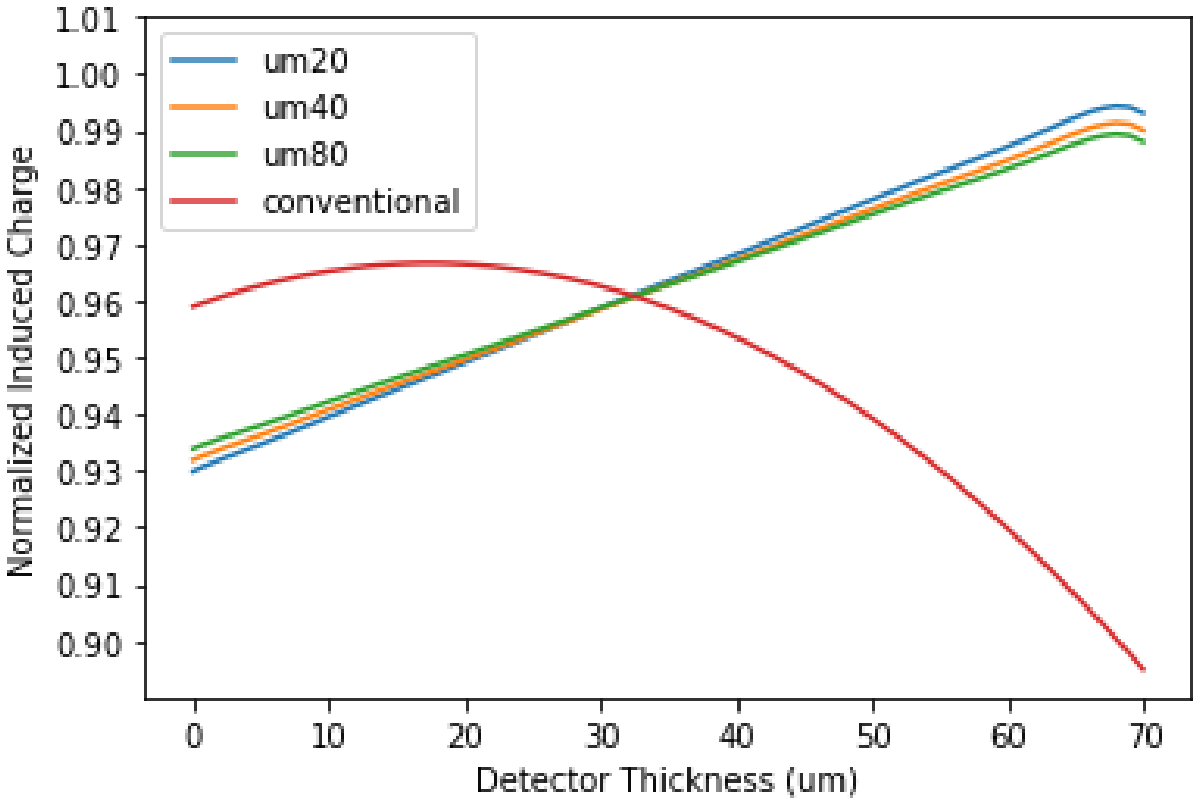

Figure 2.9: Calculated charge induction efficiencies graph with respect to detector thickness for the electrical parameters presented in literature

2.6 Pulse Height Spectroscopy

Pulse-Height Spectrometry is a technique that involves analyzing the amplitude of signals received from a detector, which are then sent to the Pulse Height Analyzer (PHA) for acceptance or rejection. In order to understand how energy is transferred in the device an assumption will be made and that interactions will occur at the photoelectric and Compton scatter levels.

When a photoelectric interaction occurs, all of the gamma energy is usually absorbed, and pulse-heights are generated within the photoconductor are proportional to the energy

deposited. Ideally, this produces a single narrow line in the pulse height spectrum, which is known as the photo-peak. On the other hand, when Compton scatter occurs, only part of the energy is deposited in the photo-conductor, specifically that which is absorbed by the deflected electron. The photo-peak created by this interaction is less than the photo-peak generated from the photoelectric effect, and a second gamma ray is produced, which is absorbed by the photo-conductor and creates a photo-peak significantly less than the peak generated from the photoelectric effect. All Compton interactions will generate photo-peaks below the photo-peak generated from the photoelectric effect.

Let's imagine a scenario where a monoenergetic γ -ray source is positioned in front of a radiation detector. We can assume that the energy of the γ rays, known as E_γ, is lower than 1.022 MeV, which means that pair-production interactions will not occur. The main γ-ray interactions with the detector will be through photoelectric absorption and Compton scattering. Most of the photoelectric interactions will cause full deposition of the γ-ray energy in the detector, with the characteristic x-ray typically being absorbed in the detector as well. The amplitude of the pulses resulting from these events is directly proportional to E_γ, as shown in Figure 2.12. If an ideal radiation detector were used, a single narrow line would appear in the pulse-height spectrum, referred to as the photopeak, at a position that corresponds to the γ-ray energy E_γ, as illustrated in Figure below.

In Compton scattering, only a portion of the γ-ray energy is transferred to the detector via the Compton recoil electron. If the scattered γ-ray is absorbed in the detector, a pulse in the photopeak is produced. However, if the scattered γ-ray escapes, the energy deposited in the detector will be less than E_γ. Based on Equation below, the energy deposited in the detector in a single Compton scattering event varies from almost zero (in the case of small-angle scattering events) to a maximum value E_{ce}, which corresponds to the energy of the recoil electron for 180-degree Compton scattering events.A potential scenario is that a γ-ray that has undergone Compton scattering could potentially undergo further Compton scattering interactions within the detector. The outcome of multiple Compton scattering events could result in a pattern of pulses with varying amplitudes that fall within the range between the Compton edge and the photopeak, creating what is known as the distribution of pulses in the "valley."

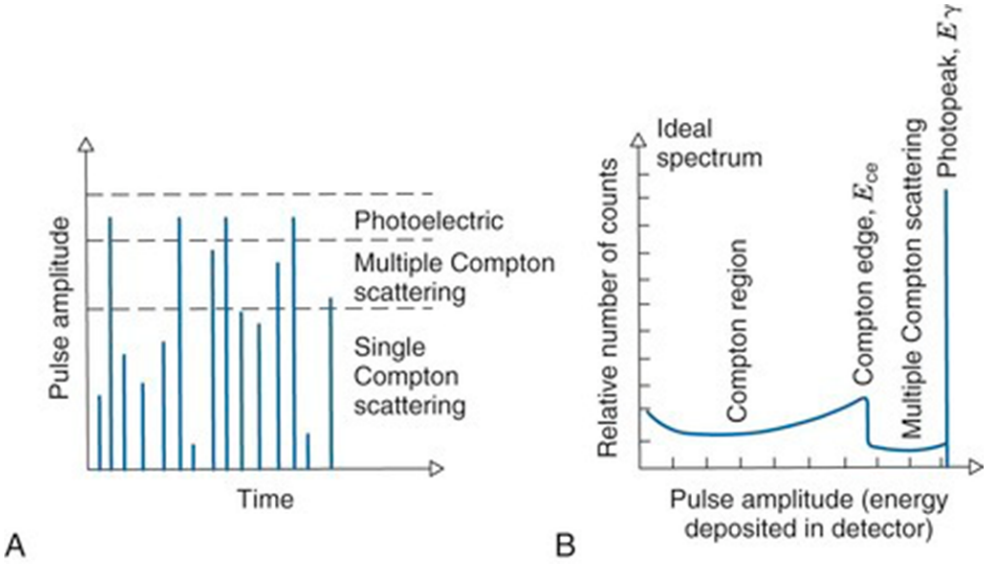

Figure 2.10: Illustration of elements due to Gamma-ray pulse-height spectrum. (A) Pulses from the detector representing different types of Gamma-ray interactions in the detector. (B) Distribution (relative number) of pulses versus amplitude (or energy deposited in the detector). Only the photopeak represents deposition of the full energy of the ray in the detector.Source[Radiology Key]

$$E_{ce} = E_{\gamma}^2/(E_{\gamma} + 0.2555) \tag{2.19}$$

Figure 2.13 shows the pulse height spectra results for the 20 micron, 40 micron and 80 micron pixels. The PHS simulations were performed using the Xenos software suite with the Gambet module. It accounts for the electric field set at 8V/um for every pixel size. The graph plots above show the that smallest pixel size i.e. 20um, has the highest photo-peak showing the highest number of photons being absorbed at 60 KeV gamma source, this is because of the fact that a smaller pixel size has a better weighting potential distribution compared to the larger sizes which allows efficient collection of charges. The

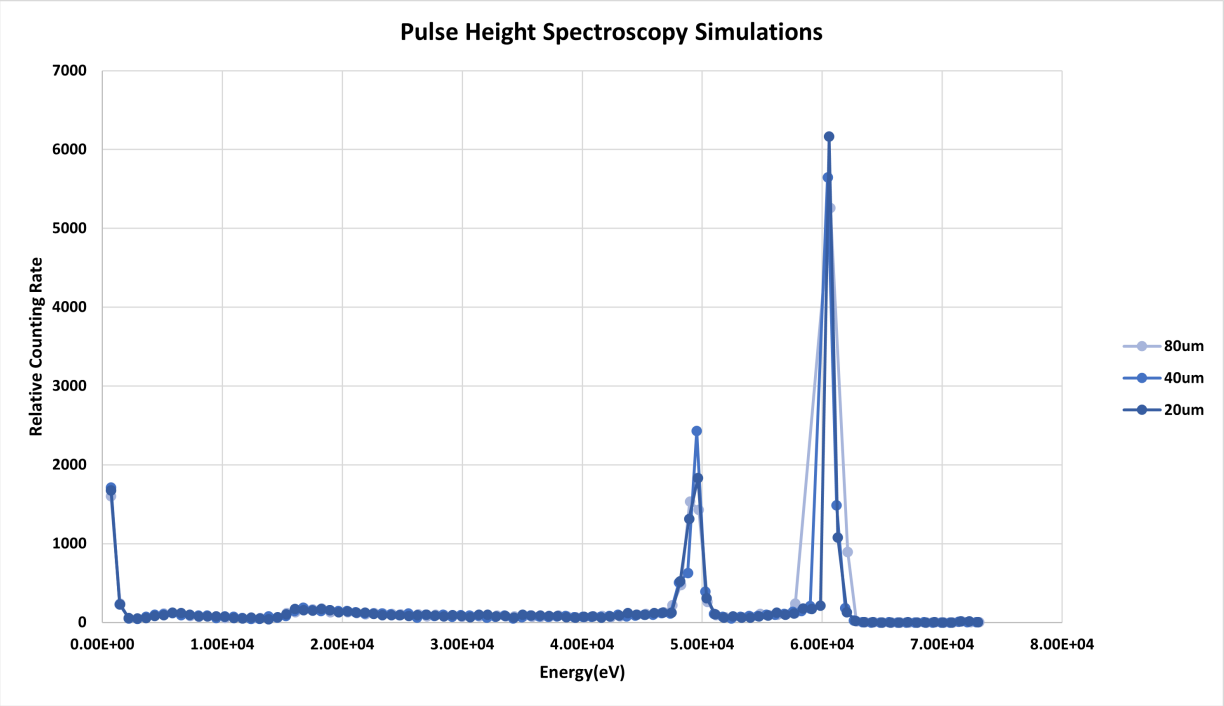

Figure 2.11: Simulated Pulse Height Spectroscopy results for different pixel sizes

higher compton edge for larger pixel can be explained by the fact that a larger area of photoconductor can be found in the 80 um pixel size which allows the production of more electron hole pairs. It can be observed that the largest pixel size, 80 microns, has the lowest photo-peak which shows the photon count rate at 60KeV decreasing with the decrease in the pixel size. Increasing the electric field can increase the absorbed photons and resolve the issue but it is to be noted that increasing the voltage at the metal grids also increases the chances of a higher charge being injected from the grids to the collecting pixel electrodes. A high voltage on the top electrode can result in the breaking down of the photo-conductor layer which can cause an avalanche breakdown.

2.7 Energy Resolution

Certain medical imaging techniques, such as dual energy subtraction used in mammography, necessitate the measurement of the energy distribution of the radiation used [147, 148, 149]. In these cases, the efficacy of the radiation detectors is typically determined by their capacity to accurately distinguish the energy distribution or spectral data of the X-ray or gamma-ray photons that are transmitted through the object being imaged. The response function of a radiation detector for a given energy is defined as the energy spectrum measured by the detector. This definition applies to all radiation detectors, including those used in other fields such as gamma-ray astronomy, nuclear spectroscopy, and non-destructive testing. The energy resolution of a detector is determined by its response to a mono-energetic source of radiation. In an ideal scenario, the response function of a detector would be a delta function. However, in reality, it is described by a Gaussian distribution due to the noise added by the electronic system and a statistical error caused by the fluctuation of pulse to pulse, even when the same energy is deposited for each event. When the fluctuation is minimal, the response function of the detector approaches a delta function, resulting in a narrower response. Figure 4.5 displays two response functions for two different detectors, one with good resolution and the other with poor resolution. The areas under the spectra should be equal since the same number of photons are absorbed by both detectors.

Although both distributions are centered at the same mean value, $E0$, the distribution obtained by the detector with poor resolution is considerably wider. This indicates that the poor resolution detector is incapable of accurately resolving specific details regarding the incident energy of the radiation. The full-width at half-maximum (FWHM) is the most frequently used energy resolution metric, as defined by [84]:

$$ER = \frac{\Delta E}{E_0} \times 100\% \tag{2.20}$$

The FWHM of the full energy peak in a measurement is denoted by ΔE, while E_0 refers to the center or photon energy that is being measured. Assuming the formation of

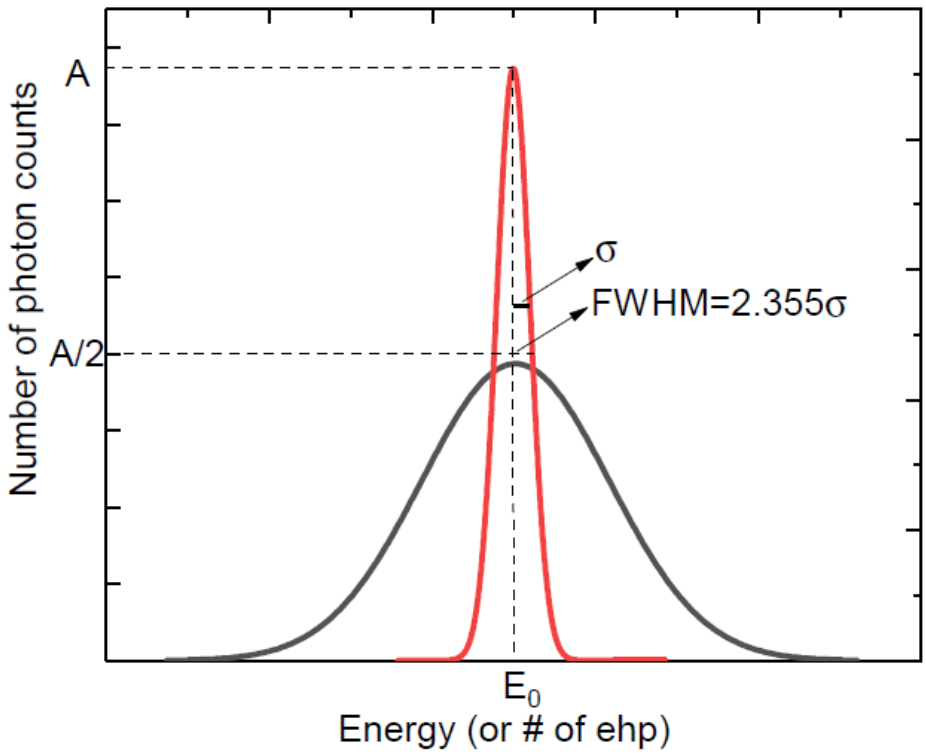

Figure 2.12: Illustration representing energy spectrum with red showing a good energy spectrum and black being poor one. [1]

charge carriers follows a Poisson process, and an average of N charge carriers are created, the expected statistical fluctuation is the standard deviation, $\sqrt{N}$. If this is the only source of fluctuation in the signal, and N is a large number, the detector's response function can be modeled by a Gaussian function, as follows [84]:

$$G(E) = \frac{A}{\sigma\sqrt{2\pi}} e^{\frac{(E-E_0)^2}{2\sigma^2}} \tag{2.21}$$

$$FWHM = 2\sqrt{2ln2\sigma} \approx 2.355\sigma \tag{2.22}$$

where A can be defined as the area under the curve and σ can be described as the

standard deviation. Since the response of majority of the detectors can approximately be linear, the average amplitude of the pulse can be described by $E_0 = KN$, where K is a proportionality constant. Then, the standard deviation, σ, of the peak in the pulse height spectrum can be given by $\sigma = K\sqrt{N}$, while its FWHM will be $2.355K\sqrt{N}$. Hence, the energy resolution can be given as [84]:

$$ER_{poissonLimit} = \frac{2.355K\sqrt{N}}{KN} = \frac{2.355}{\sqrt{N}} \tag{2.23}$$

The equation shows that the achievable energy resolution is dependent on the total number of generated charge carriers. To attain an energy resolution lower than 1%, it is necessary to generate over 55000 EHP through a photoconductor. The theoretical calculation highlights the importance of generating as many EHPs as possible per event to achieve a low energy resolution limited by the total number of EHPs generated. Despite this, precise measurements, minimizing system noise, and achieving intrinsic response through radiation detectors have shown that energy resolution at least one order of magnitude better than predicted by the statistical argument is achievable. These results indicate that the formation of each charge carrier is not independent and cannot be represented by simple Poisson statistics. The Fano factor (F) was introduced to address this issue, quantifying the difference between the statistical fluctuation defined by the Poisson process and that obtained through experimentation, defined as [85].

$$F = \frac{observedvariationinN}{Poissonpredictedvariance(=N)} = \frac{\mu}{\sigma^2} \tag{2.24}$$

By including the Fano factor, F, and re-arranging the energy resolution formula the equation becomes:

$$EnergyResolution_{PoissonLimit} = \frac{2.355K\sqrt{N}\sqrt{F}}{KN} = 2.355\sqrt{\frac{F}{N}} \tag{2.25}$$

The energy resolution is scaled by a factor of$\sqrt{F}$. While scintillator detectors primarily adhere to Poisson statistics for energy resolution, with a Fano factor of one, semiconductor

detectors exhibit better energy resolution than what Poisson statistics would predict, due to a Fano factor that is significantly lower than one. In particular, the Fano factor for CZT and silicon detectors have been measured at 0.089 and 0.01, respectively, indicating that these detectors are capable of achieving excellent energy resolution, as reported in [86].

Ideally, a pulse-height measurement system should detect pulses of the same amplitude for the same amount of photon energy deposited. However, this is not practically achievable due to various noise and interference sources present in both the detector and the measurement system. These include drifting of detector operation characteristics, electronic noise, and statistical fluctuations resulting from the discrete nature of the signal being measured. There are two significant sources of statistical fluctuations, namely: 1) loss of energy due to vibration in the crystal that results in not all deposited photon energy being utilized for generating free charge carriers, and 2) the loss of some generated charge due to trapping and recombination, leading to incomplete collection.In most radiation detectors, statistical noise is the primary source of noise and sets the lower limit for achievable detector performance. Even if some of the noise sources follow other distributions, according to statistical theory, if the noise sources are systematic and independent, the overall response function will always tend towards a Gaussian shape. As a result, the total full width at half maximum (FWHM) of the detector response can be determined by adding the FWHM values of each individual source of fluctuation in quadrature, as demonstrated below:

$$(FWHM)^2_{overall} = (FWHM)^2_{statistical} + (FWHM)^2_{noise} + (FWHM)^2_{drift} + ... \quad (2.26)$$

The energy resolution from the PHS simulations performed were calculated to be at 5% to 2% ranging from the 80 micron to the 20 micron pixel structure size.

Chapter 3

Fabrication and Characterization of Unipolar Charge Sensing X-ray Detector

3.1 Fabrication Procedure for Unipolar Charge Sensing X Detector

Wide band-gap polycrystalline and amorphous photoconductors which are operated at room temperature have proven to effective alternatives compared to single-crystalline photoconductors [87, 88, 89, 90, 91]. Over the years, amorphous Selenium (a-Se) has been developed and used commercially for X-ray imaging applications like tomosynthesis and mammography [8, 61, 91]. The timely detection of calcification in the breast is crucial for diagnosis signals as an early warning for breast cancer. Amorphous Selenium based detectors serve as an effective direct conversion photoconductor which has proven to have a high spatial resolution that allows the timely tracing of calcification inside the breast. A-Se proves to be a reliable and low-cost solution allowing fabrication for large area readout circuitry. However, applications pertaining to X-ray photon counting for higher spatial

resolution like enhanced-contrast spectral mammography, cannot be implemented using the conventional A-Se detector structure. The work in this chapter discusses the design of and fabrication of unipolar charge sensing A-Se Single X-ray detector.

The unipolar charge sensing structure was fabricated in 4 different pixel sizes ranging from 20 microns to 150 microns in the Giga-to-Nano laboratory at the university of Waterloo. This chapter discusses all the fabrication processes that the wafers went through to fabricate the unipolar charge sensing detectors and also includes the experimental results that were achieved through.

3.2 Photomask Design

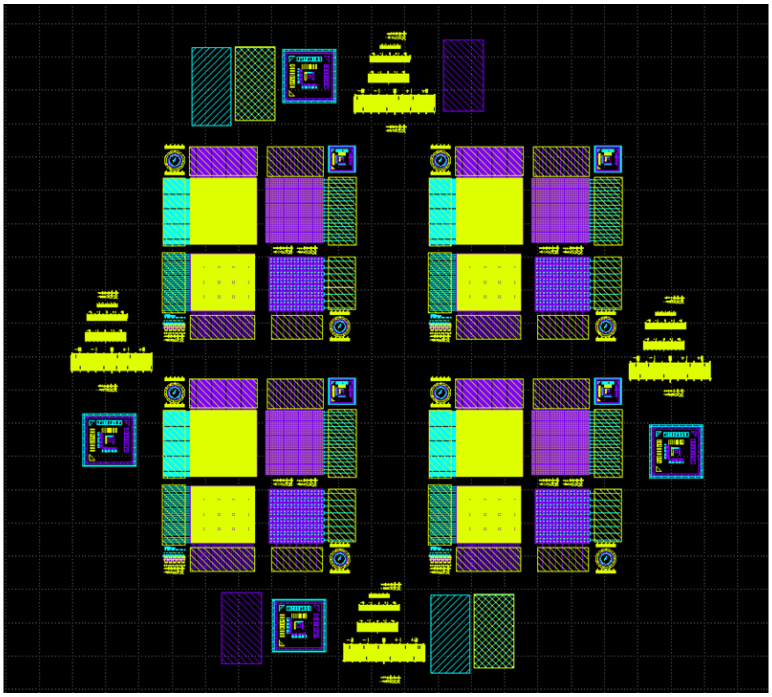

Figure 3.1: Photomask layout of the designed unipolar charge sensing detector

A photomask is made up of a glass or quartz substrate material having a patterned opaque layer deposited on top of the substrate. This causes some regions to be opaque while

the remaining regions are allowed to be transparent which allows light to pass through. The photomask is used in the photolithography process in which it is placed next above a substrate wafer which is covered with a photosensitive layer also known as photoresist. As the UV rays are allowed to pass through the photomask the opaque and transparent regions allow to replicate the pattern on the photomask to the substrate wafer for further fabrication.The unipolar charge sensing detector was made using a three mask process. The five inch chrome masks were desgined using K-layout software and was fabricated at the nanofabrication facility at the university of Alberta.

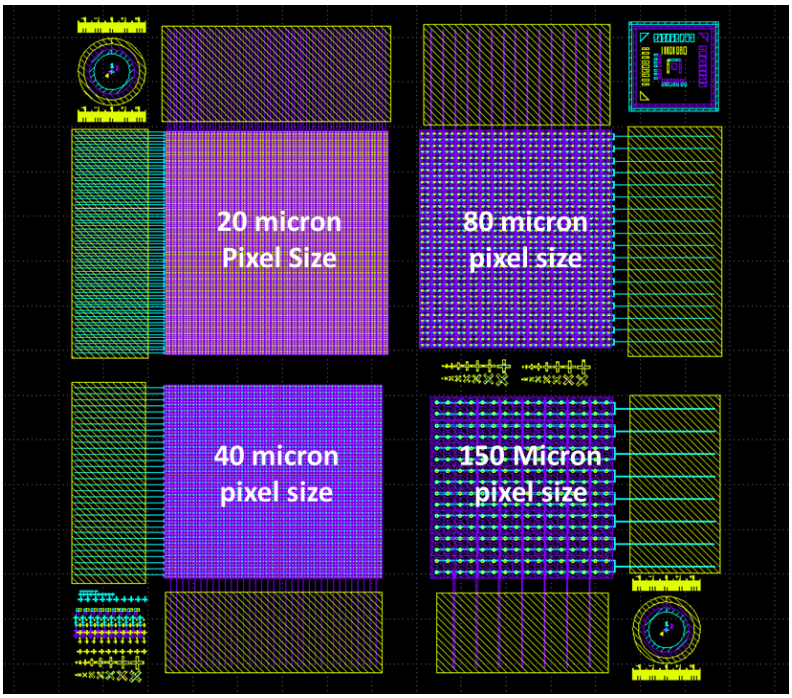

Figure 3.2: A close up view of the photomask design showing different pixel sizes of the designed x-ray detector

The first mask design includes the collecting pixel electrode design along with the tracks linking each pixel row together. This mask includes the 4 different pixel sizes ranging from 20 micros to 150 microns. The second mask includes the design for the metal grid electrodes for each pixel which surrounds each collecting electrode pixel. This mask also includes the signal tracks connecting each metal electrode column wise. The third

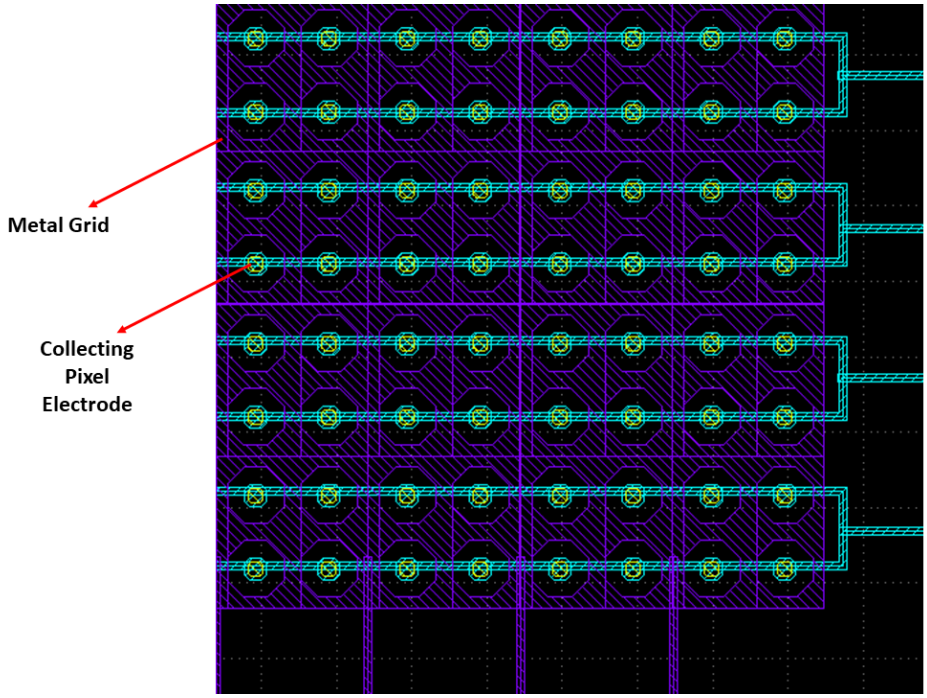

Figure 3.3: Zoomed-in view of the photomask design showing metal grid and collecting pixel electrode

photo-mask includes the design for the via-opening required between the photo-conductor material and the collecting electrode for efficient charge collection. The images below show the mask designs for our work. Different alignment marks are also included in each design to allow for the accurate alignment during the photo-lithography process.

3.3 Wafer Cleaning

The Corning Eagle XG(regd.) glass was selected as the wafer substrate for the fabrication of the device. Eagle XG is an alkaline earth boro-aluminosilicate glass material. The thermal coefficient of eagle XG is low which makes it a good option for high temperature processing. The eagle XG substrate is also alkali free. The wafer was circular in shape having a 4 inch diameter and a thickness of 0.7mm.

The wafer was cleaned using the RCA-1 process also referred to as standard clean-1 which was developed at the RCA laboratories in the 1960's by Werner Kern[refs from UC Irvine RCA 1 Docs]. The procedure was designed to remove organic films and residue from the surface of the silicon or glass wafers. The decontamination process involves the subsequent oxidative desorption and complexing with a solution constituting of Hydrogen peroxide, Ammonium Hydroxide and deionized water. The RCA-1 solution was made with 5-parts of DI water, 1 part of Ammonium Hydroxide (NH_4OH) and 1 part of Hydrogen peroxide (H_2O_2). The solution was then heated to 70 degrees celsius in Pyrex beaker on a hot plate. Once the solution started to produce bubbles vigorously the wafers were soaked in the solution for 15 minutes. Once finished, the wafer was transferred to another beaker and soaked in overflowing DI water. After sometime the wafer was taken out and was blown dry using nitrogen gas. An important step after wafer cleaning is to dry the wafer. Any left over water marks after the drying of the wafer can cause particle recontamination because of static charges. The drying methodology in this work involves the blowing the wafers with dry nitrogen gas followed by heating them up on hot plates to remove any remaining water droplets. After the cleaning and drying process the wafers were transferred to wafer cassettes for storage which were always kept inside the cleanroom.

3.4 Metal Sputtering

Sputtering refers to the process of removing atoms from a surface due to particle bombardment. This leads to the eventual ejection of atoms from the surface. Although sputtering technically only refers to the interaction between ions and a surface, it is commonly used to describe the entire deposition method.

A typical magnetron sputtering system is depicted in Figure 3.4. The main component is a vacuum vessel where the air is evacuated to a high vacuum level at 1×10^6 Torr. A process gas is then introduced into the chamber, and the flow is regulated to maintain the desired pressure range, typically between 1-40 mTorr. Argon is commonly used as a process gas due to its inertness, availability, and affordability.

In a DC setup, the target material is connected to the negative terminal of a power supply, which generates a self-sustained glow discharge. This discharge serves as the source of positive ions, which are attracted by the negative potential at the target. As the ions approach the surface, they are accelerated to high energies and gain energy in the high electric field region near the target. When the ions collide with the surface, they produce a collision cascade that removes atoms from the surface. This collision also extracts electrons from the surface, which are then accelerated towards the discharge and participate in the ionization of additional atoms. The ionization efficiency is significantly increased by a static magnetic field that confines electrons to a region near the target.

Finally, the sputtered atoms travel across the plasma and deposit onto the substrate and the walls of the apparatus. The WLOS cluster sputtering system in the giga-to-nano lab was used for the deposition of chrome and aluminum metals on to the designed devices. The WLOS sputtering system can provide a maximum deposition on an area of 39 cm x 27 cm. The 4 inch circular substrate holders were used to deposit Chromium and Aluminum metals using direct current power supply. The deposited metal thickness was for both the metals was kept at 100 nano meters. The fabrication step also involved the deposition of a thin Aluminum layer at 50 nano meters which was used as a etching mask for the RIE process. This deposition was also performed using the WLOS clutter sputtering system. Figure 3.5 shows the WLOS sputtering system in G2N that was used to deposit the metals on the substrates.

3.5 Photolithography

The lithographic process involves creating patterns on a substrate by transferring patterns from a mask or reticle. The mask contains opaque and transparent regions in a binary arrangement. The opaque regions are created by coating a highly absorbing material on selected areas. Illumination is applied on the mask, and only the transparent regions allow light to pass through.The transmitted light is absorbed by a photosensitive film, known as a photoresist, on the surface of the substrate. The photoresist undergoes a

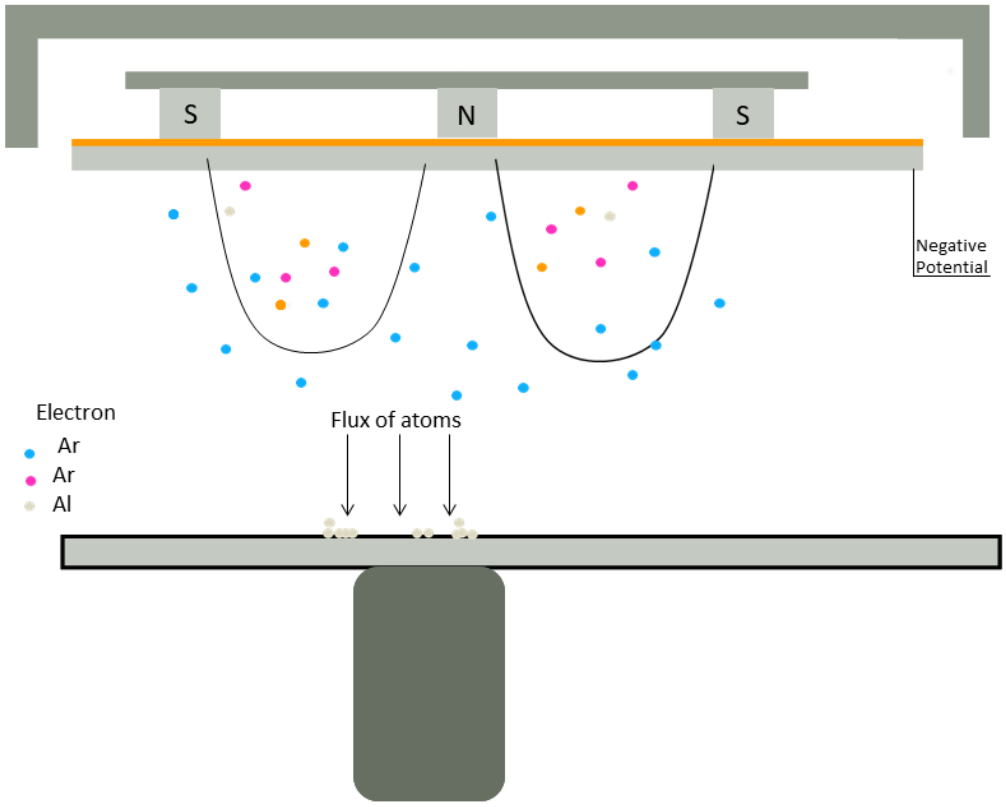

Figure 3.4: Illustration of a typical magnetron sputtering system process involves creating a glow discharge between two electrodes in a low-pressure environment (typically between 1-100 mTorr). The negatively biased electrode, also known as the target, attracts argon ions from the discharge. As a result, some atoms from the cathode are vaporized and travel towards the substrate where they get deposited. The magnets placed behind the target serve to confine electrons, thereby increasing the efficiency of the process.[2]

photochemical reaction when exposed to light, which alters its solubility. If the exposed portion of the photoresist becomes soluble in a developer, the resist is positive tone. If the exposed portion becomes insoluble, the resist is negative tone.After development, the remaining photoresist serves as a barrier against a subsequent plasma etching. The open

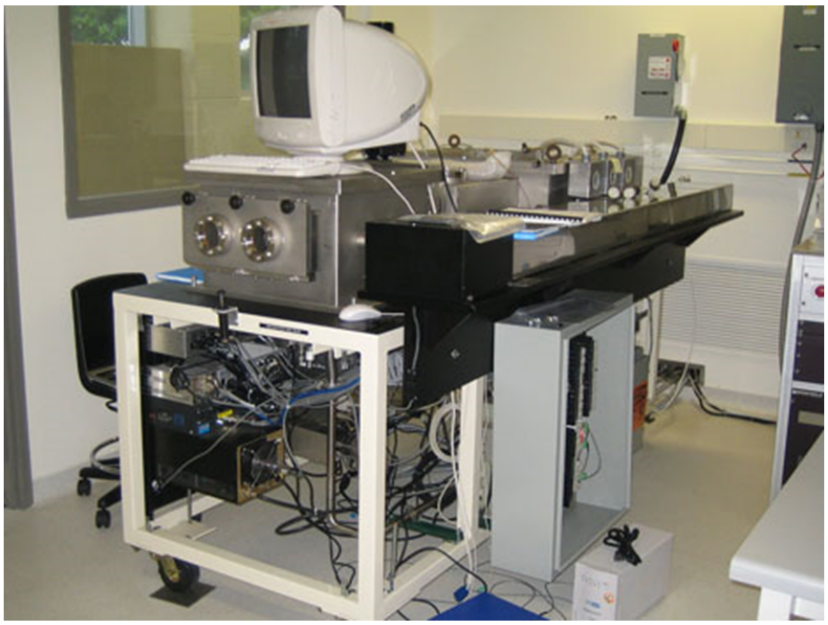

Figure 3.5: Image of the WLOS cluster sputtering system in the G2N lab used in this work

regions of the photoresist can then be transferred into the underlying film, allowing for pattern transfer of the resist pattern into metals and oxides, which cannot be patterned directly by irradiation.This process is used in the fabrication of electronic devices such as microprocessors, memory chips, and sensors, where precise patterning is necessary for the device to function correctly.

The photolithography process is comprises of several steps namely: surface preparation, spin coating, pre-baking, mask alignment, light exposure, development, post-baking.

3.5.1 Surface Preparation

The surface preparation can be described as the cleaning of the wafer and the removal the contaminants and residues before coating photoresist on the glass wafer substrate. Adhe-

Figure 3.6: Image of the SUSS MA6 mask aligner present in the G2N lab

sion promoters are used to increase the adhesion between the substrate and photoresist. Primers are used which can form bonds with the wafer's surface. For this work, we used Hexamethyldisilzane (HMDS) which was spin coated on top of clean glass substrates before the coating of photoresists.

3.5.2 Spin Coating

Centrifugal force is employed in spin coating to create even thin films. The process begins by securing a wafer onto a spindle. A liquid solution containing nanoparticles or precursors is then released onto the center of the substrate using a syringe. The substrate is then subjected to centripetal acceleration, causing the liquid to spread evenly over the surface due to centrifugal force. As a result of excess material being thrown off the edge of the rotating substrate, a uniform thin film is left on the surface. This method is widely used

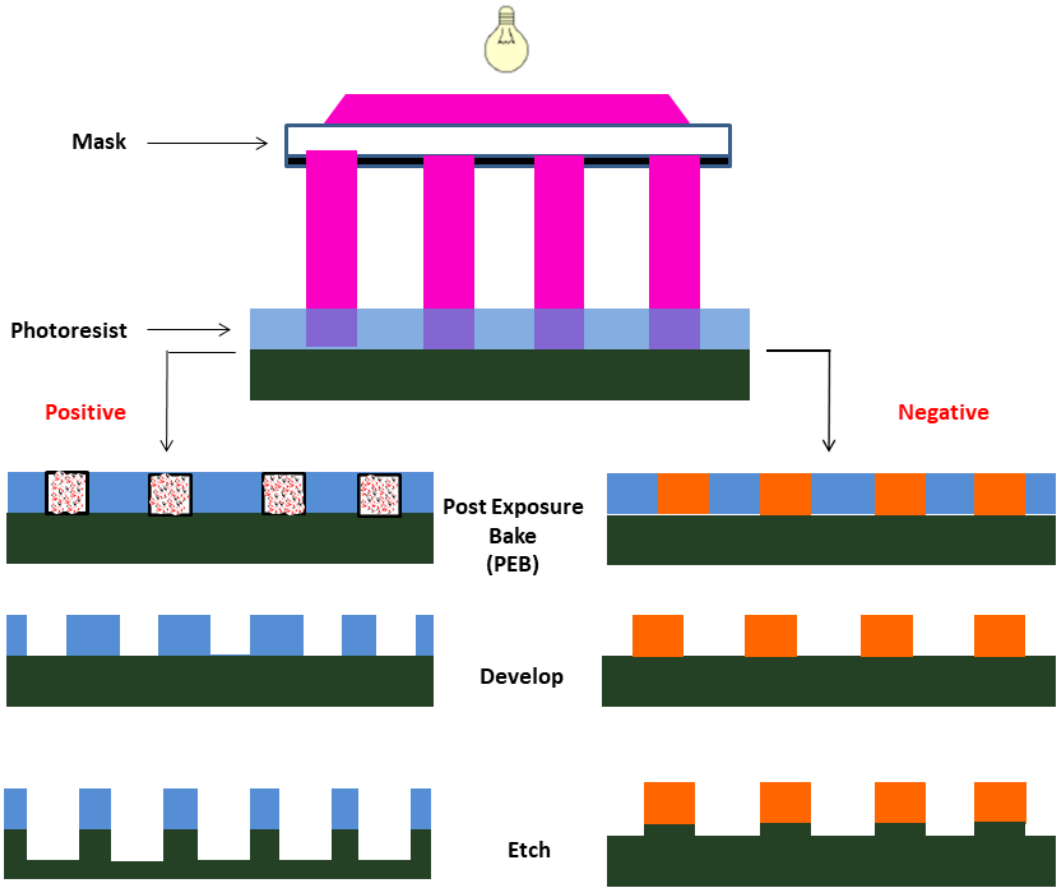

Figure 3.7: Illustration showing the typical photolithography process using positive and negative photoresist

to create consistent thin films in various applications.In spin coating, the speed at which the substrate rotates must be carefully controlled relative to various material properties of the solution. Viscosity is particularly important because it determines the resistance to uniform flow, which is essential for achieving a uniform surface finish. Depending on the viscosity of the solution, spin coating can be performed at speeds ranging from 500 to 12,000 revolutions per minute (rpm).While viscosity is the most critical material property in spin coating, other factors such as surface tension and percent solids can also affect the flow characteristics of the solution and the desired thin film thickness needed to achieve specific

end-use properties, such as electrical mobility. Spin coating is therefore conducted with a comprehensive understanding of the relevant material properties and plenty of adjustable parameters to suit specific characteristics such as flow, viscosity, and wettability.

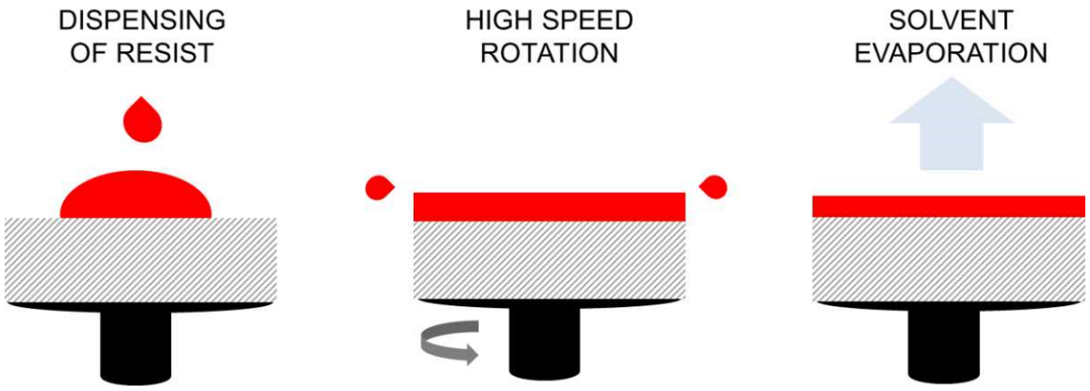

Figure 3.8: An Illustration showing a general spin-coating process. source [insecto.co.uk]

After spin coating HMDS on to the wafer the photoresists were spin coated to prepare the wafer for the photolithography process. The fabrication process for the device in this work required photolithography at three different steps. For each step positive/ negative photoresists were selected as per the requirements. For the negative photoresist we used AZ nlof 2035 and ——— was used as the positive photoresist. The spin coating process was also used to coat PI layers on to the wafer as well.

3.5.3 Post baking

The last after spin coating the photoresist on to the wafer is post baking the wafer on the hot plate which sometimes is also referred to as hard baking. This causes the photoresist on the wafer to harden up. This is done to prevent the photoresist to come off easily during the etching process. For post baking the temperature is normally set 5 to 15 degrees celsius higher to that for soft baking. It is possible to observe some shrinkage in the spin coated photoresist layer following the post bake process.

3.6 Wet Etching

Wet-etching techniques rely solely on chemical reactions and are typically highly selective. However, they are mostly isotropic, meaning that the liquid solution wets both the lateral and bottom surfaces of the structures being etched. Anisotropic etching, in which different crystallographic planes are removed at varying rates, can only be achieved in crystalline materials.

Occasionally, wet-etching processes require strongly basic or acidic solutions, or temperatures well above room temperature. In these situations, the resist may not provide adequate masking due to issues such as the resist's dissolution or adhesion problems. The resist and the sample are only held together by Van Der Waals forces, which may not be sufficient to withstand the high forces created during the etching process. Due to which the etching chemical can sometimes damage the interface region which causes the separation of the resist layer. In this case, another material is deposited on top of the photoresist which serves as etching mask for the process. Wet etching was performed after every step where the wafer was exposed to UV for photolithography. In this work we used wet etching the etch the chrome and aluminium metals to produce the desired pattern for our x-ray detectors. Chrome metal was used to produce the pixel electrodes in this work while we used Aluminium metal to produce the grid metal for the x ray detector.

Figure 3.9: An image showing the wet bench station by FineLine Fabrications in the G2N lab

3.7 Reactive Ion Etching

The method of dry etching involves a process known as Reactive Ion Etching (RIE). RIE is a type of dry etching that combines chemical reactions with directional ion bombardment in a vacuum chamber. One common configuration of RIE is the parallel plate reactor, as depicted in Figure 1. The top electrode is connected to the "shower-head," which is the inlet for the etching gas, and is grounded. The wafer is placed on the bottom electrode, which is connected to the RF power generator and serves as the power electrode.When an electric field is applied to a gas, it ionizes the gas molecules and creates plasma. Once the discharge is ignited and plasma is established, a DC bias voltage is formed on the RF-powered bottom electrode. This DC bias voltage extracts ions from the bulk plasma and energizes them, contributing to the directionality of etching and desorption of reaction byproducts from the wafer surface. The generation of reactive species in the bulk plasma,

including excited molecules and radicals, as well as the density of charged species such as ions and electrons, depend on the applied RF power. Therefore, the DC bias and ion current to the substrate are interdependent and controlled using the same RF power source.

This work uses reactive ion etching for etching and developing the polyimide layer which plays an important role as a hole blocking layer in the detector.

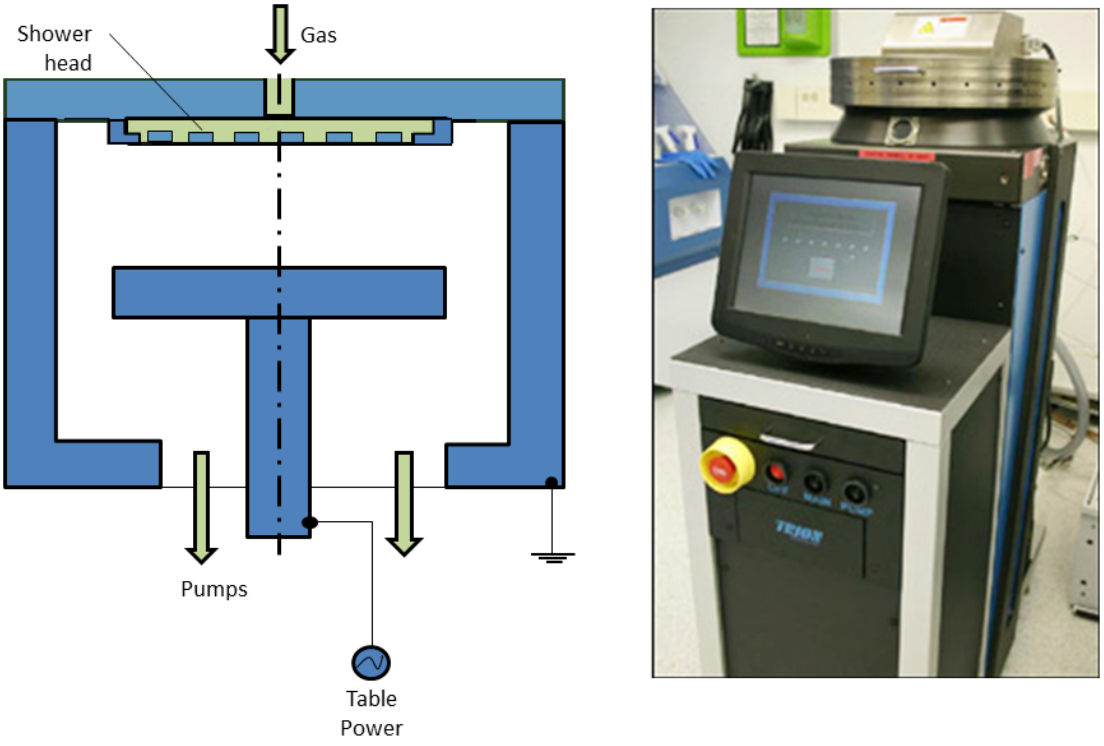

Figure 3.10: A figure showing a typical reactive ion etching system (left). An image showing the Phantom II reactive ion etching system in the G2n Lab

3.8 Fabrication Process

The fabrication process starts off with by cleaning the glass wafers through the RCA cleaning process after which they were dried using nitrogen gas and then stored safely in wafer carriers inside the Giga-to-Nano lab at the university of Waterloo. After the cleaning process the 2nd step was to deposit a chrome layer of thickness 100 nm using the DC metal sputtering tool. The wafer was then washed with acetone, IPA and DI water. The wafer was then spin coated with HMDS to improve the adhesion of the negative photoresist (nlof-2035) on to the wafer. The spin coater was set at an intial rpm of 500 at an acceleration of 255 m/s for 10 seconds and the final spin at 4000 rpm at an acceleration of 255 m/s for 1 min to spin coat a 3um thick layer of photoresist on to the wafer. After spin coating the wafer was soft/pre baked at 90 degrees Celsius for one min. The wafer was then exposed for 6 seconds using the UV rays of wavelength at 193 nm. The wafer is then dipped in the developer for 2 mins to remove the unexposed photoresist. The wafer was then hard baked at 110 degrees celsius for one min. Next, the wafer was dipped in the chrome etchant for 2 mins to etch away the uncovered metal layer forming the collecting pixel electrode pattern on to the wafer. After etching the wafer was dipped in water for 5 minutes. Afterwards, the wafer was dipped in stripper for 5 minutes to remove all the photoresist from the wafer. The wafer was then washed with acetone, IPA and DI water to prepare it for the next step.

After the patterning of the 1st photomask on to the wafer, the next step was to spin coat a 1.8um layer of polyimide on to the wafer. After spin coating the wafer is soft baked and hard baked at 90 and 150 degrees celsius. Next the wafer was cured at a temperature of 350 degrees celsius for 2 hours. The next phase was to pattern the metal grid layer on the wafer. This required a deposition 100 nm of aluminium layer on the wafer using DC sputtering process. Following the Aluminum metal deposition the wafer was cleaned using IPA, aceton and DI water. Next, the wafer was spin coated with HMDS again to improve adhesion of the negative photoresist on the wafer. This was followed by soft baking, UV exposure, photoresist development, hard baking using the similar methodology as was done for the first photolithography procedure. The etching and stripping process was repeated like in the previous steps and the wafer was then washed with acetone, IPA and DI water.

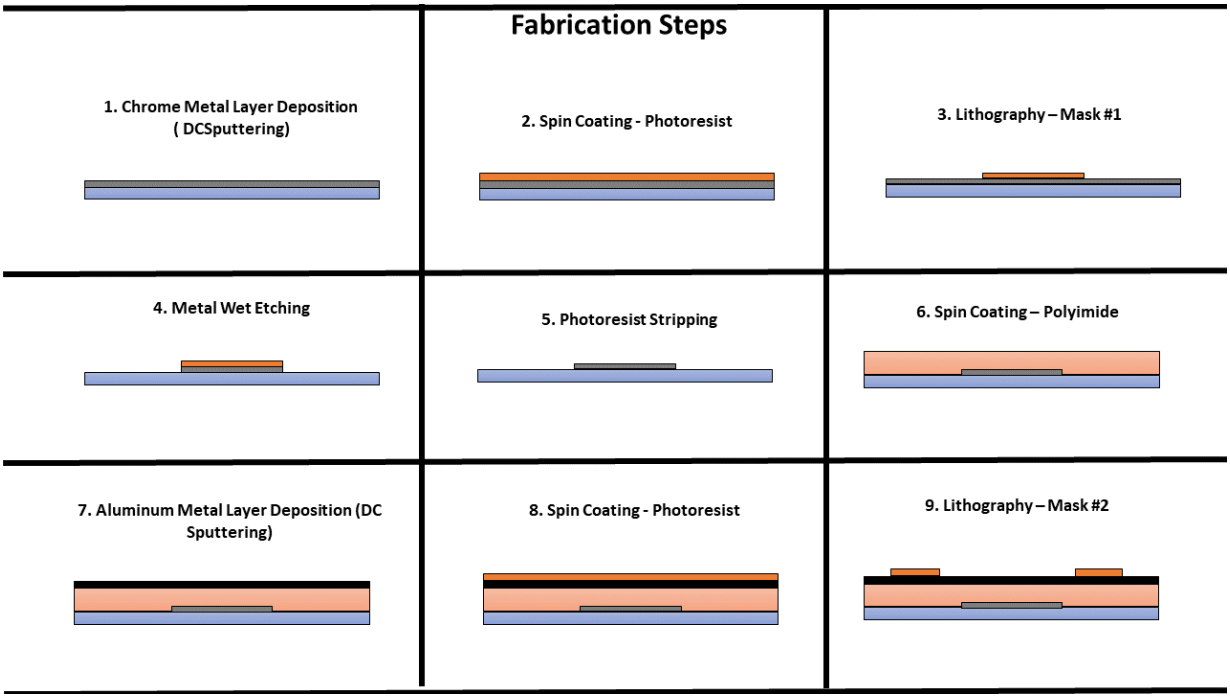

Figure 3.11: Fabrication Steps for the fabricated unipolar charge sensing detector

Next, the metal grid electrodes were needed to be covered with a 1.8um polyimide layer. This was done by spin coating, soft and hard baking and curing polyimide using the same recipe as discussed previously.

The third photo-mask was designed to open vias from the top of the device and down to the collecting electrode. The polyimide layer can be etched with oxygen gas using the reactive ion etching process. However, this process required some care as we only want to etch the polyimide layer on top of the collecting electrode. Therefore, this process required to use an etching mask. To do this we deposited a 50 nm thick Aluminum metal on the wafer using DC sputtering. The wafer was then washed with acetone, IPA and de-ionized water. Next, the wafer was spin coated with HMDS and positive photo-resist (AZ3312) having a thickness of 2um setting the spin coater at 1000 rpm. The wafer was then soft baked at 90 degrees celsius for 1 minute. The wafer was then exposed to UV light for 12 seconds. The wafer was then dipped in the developer solution for 1 min to develop the

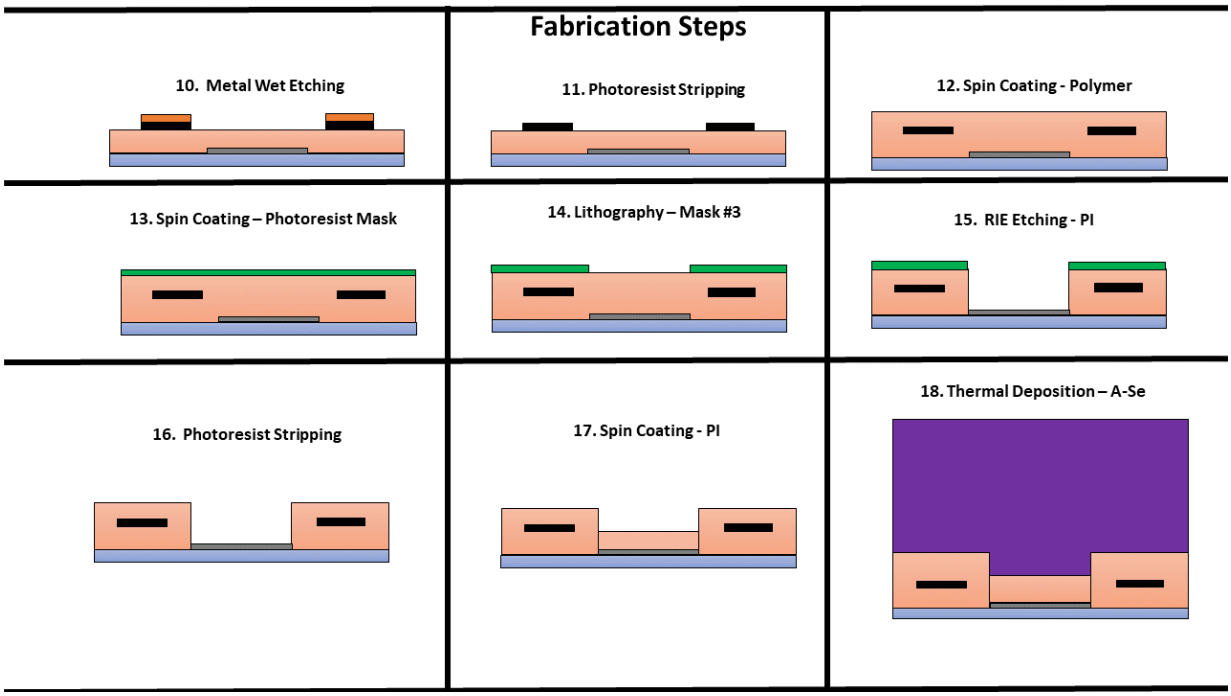

Figure 3.12: Fabrication Steps for the fabricated unipolar charge sensing detector

photo-resist. Next, the wafer was post baked at 90 degrees celsius for 1 minute. Next, we go through the wet etching process to etch the Aluminium with the Aluminum etchant for 2 minutes. The wafer was then dipped in the stripper solution for 2 mins to remove all the photo-resist layer. Next, the wafer was washed with IPA, acetone, DI water and then dried with nitrogen gas to prepare it for the reactive ion etching process. The RIE was performed to etch via holes down in the PI layer on top of the collecting pixel electrode. The RIE etching rate for PI was set at 270nm/min and hence the wafer underwent the RIE process for 7 minutes inside the chamber with oxygen gas at 50ccm. The wafer was then washed with IPA, acetone, DI water and dried with nitrogen gas. The next step was to spin coat a 1.8um PI layer on top of the wafer to prepare it for the amorphous selenium deposition. The same receipe was followed for the spin coating of PI layer as discussed previously. The next and final step was thermal deposition of a 70um a-Se on top of the wafer which would serve the purpose of the photoconductor on the device.

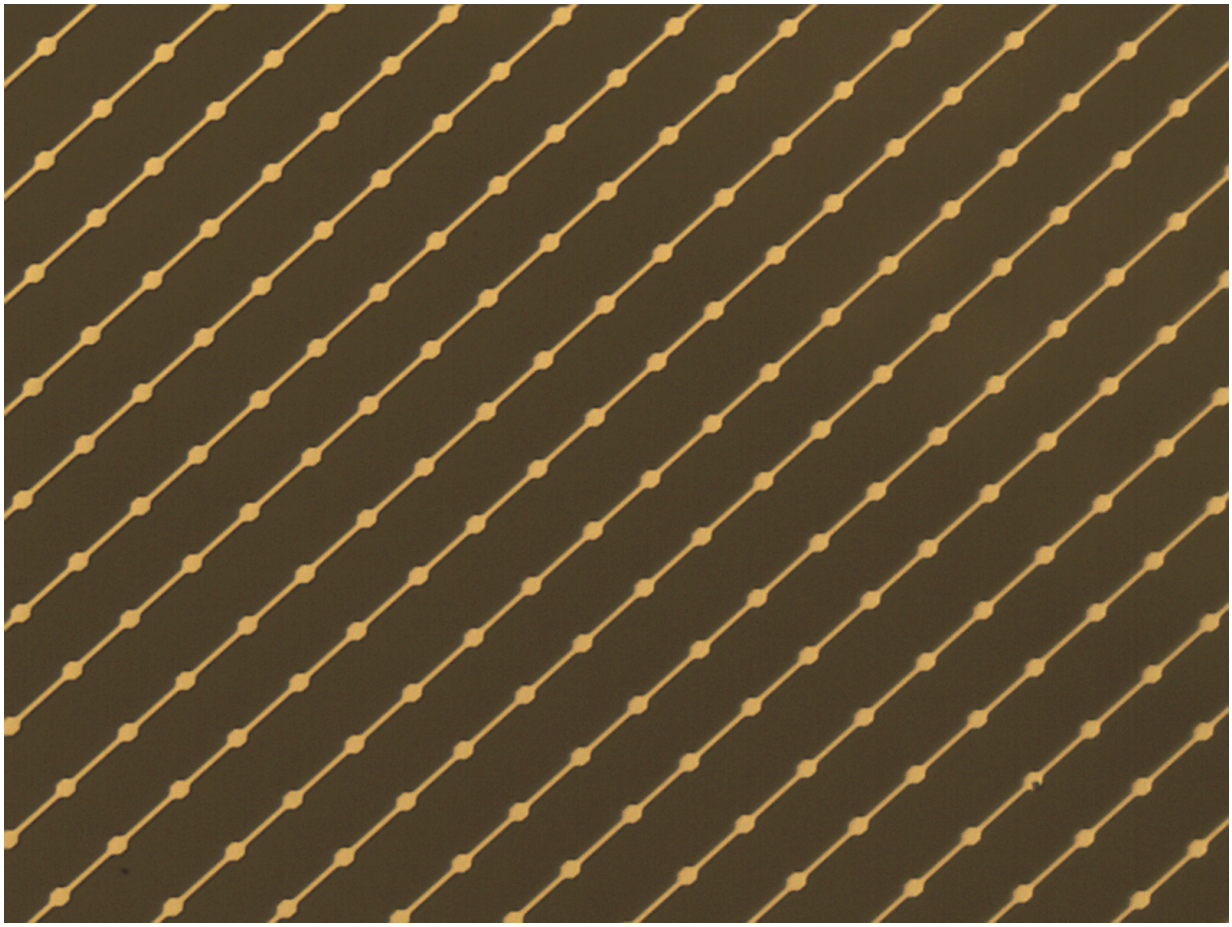

Figure 3.13: Microscopic view of the fabricated device showing the collecting pixel electrodes of 40um pixel size

3.9 Experimental Results

The device was tested for dark current and photocurrent response to verify it's performance the testing setup for the dark and photocurrent measurements involved The research conducted measurements on the dark and photo currents while keeping the applied electric field constant. To do this, we used a high-voltage power supply from stanford research systems (SRS-PS365) to apply a positive voltage on the top electrode of the device layer and a picoammeter (Keithley-6482) which were both automated to carry out the dark-current

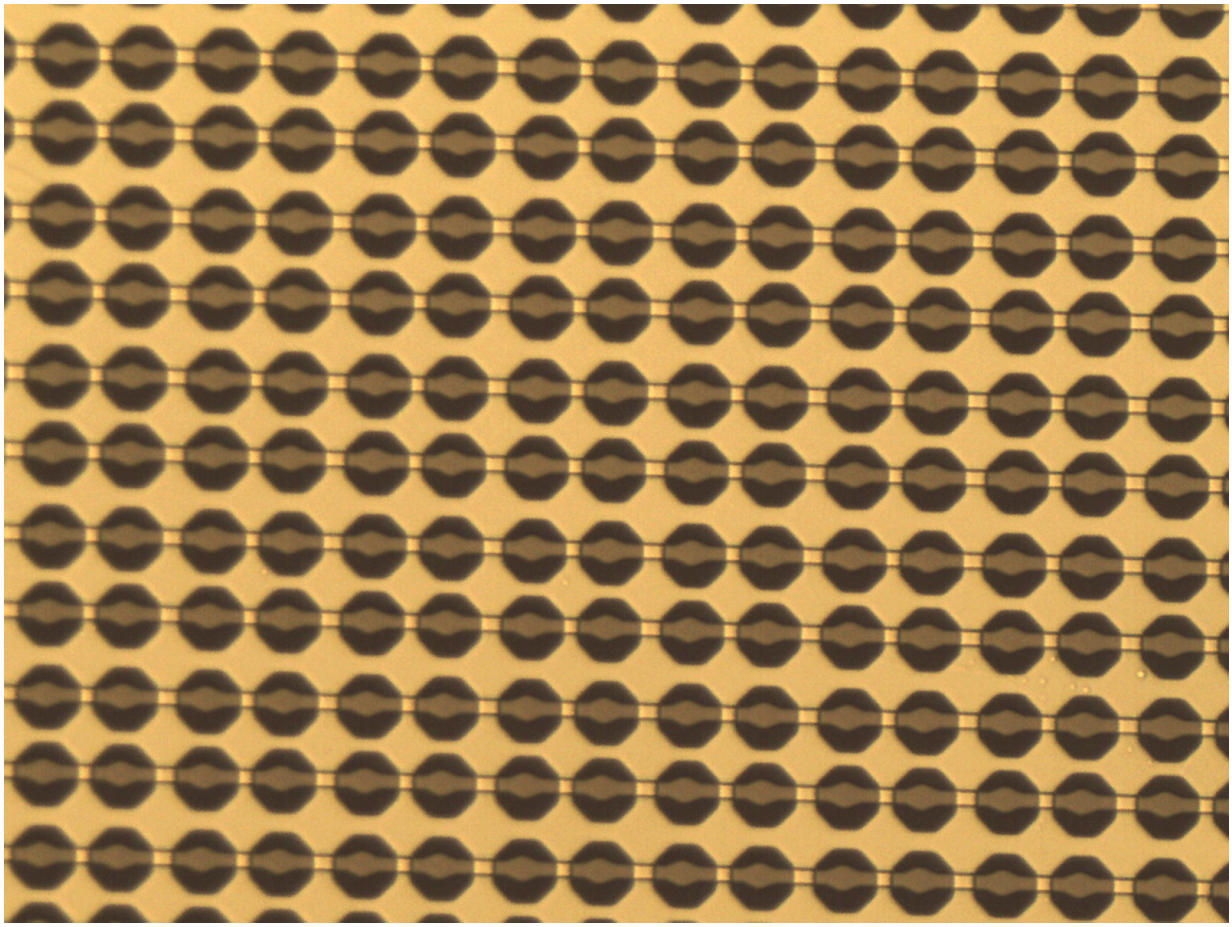

Figure 3.14: Microscopic view of the fabricated device showing the collecting pixel and grid electrodes for the 80um pixel size

measurements. The samples were kept in a short circuit configuration in a light-proof-box for at least 24 hours between measurements to ensure that any trapped charge was completely released. For the photo-current measurements, the samples were exposed to UV LED pulses. The images below show the dark current measurements for the conventional x-ray detector and the photocurrent response. For the photocurrent response the UV led had a pulsewidth of 2 seconds with a period of 3 seconds. The PI layer helps reduce the dark current in the detectors the greater the thickness of PI used the lower would be the dark current. As can be seen from the dark current plot for the conventional detector

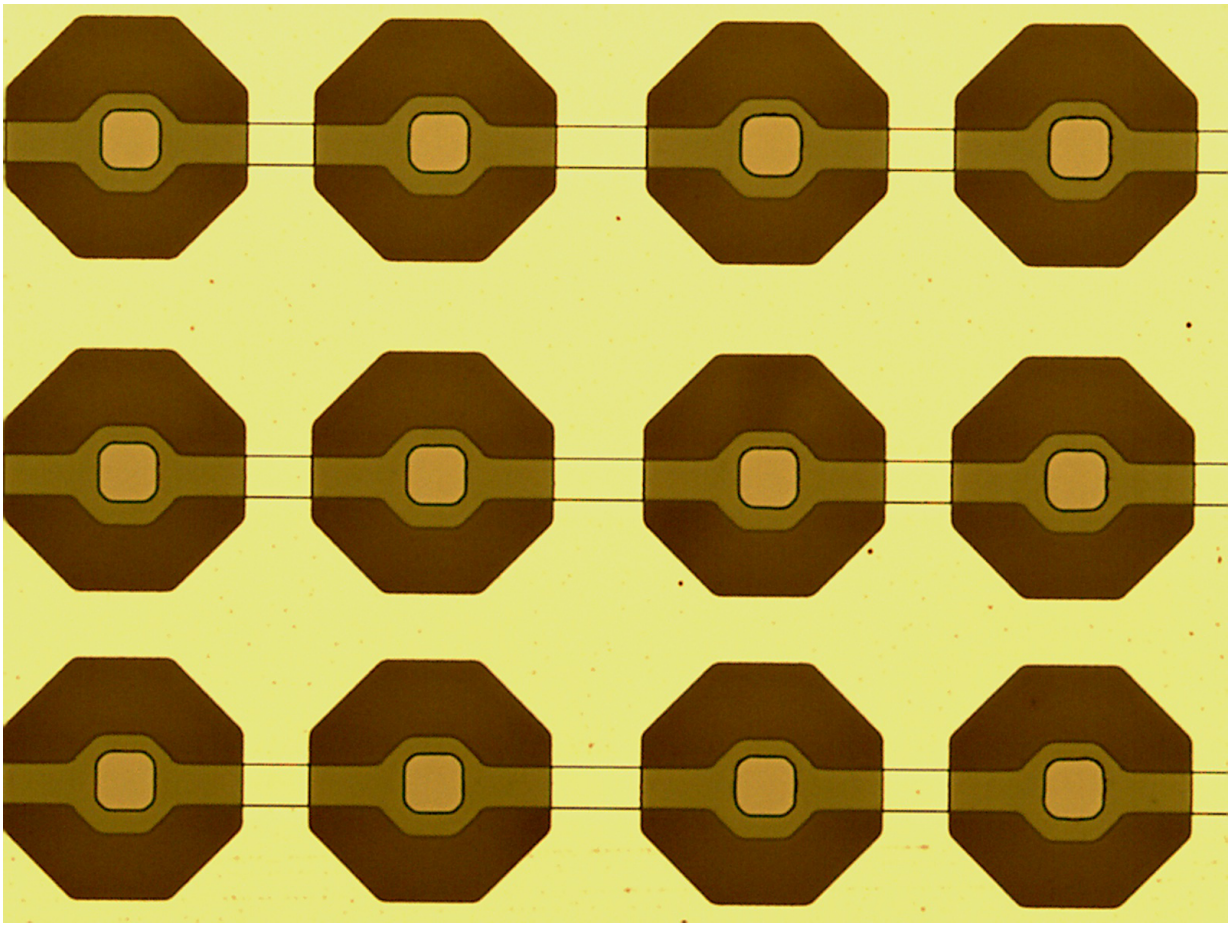

Figure 3.15: Microscopic view of the fabricated device showing the collecting pixel electrode and the grid electrode for 150um pixel size

the dark current starts at 4 pA but then gradually falls to 0 at about 5-6 minutes. The photocurrent response for the conventional detector also shows the output waveform at an average amplitude of 20 pA.

However, for the dark current measurements looking at the fabricated unipolar device shows a lesser dark current at 0.7 pA which sharply falls approximately to 0 in 5-6 minutes. The photocurrent response shows a smaller peak compared to the conventional detector mainly because it was operating at half the electric field i.e. 5V/um, than that of the

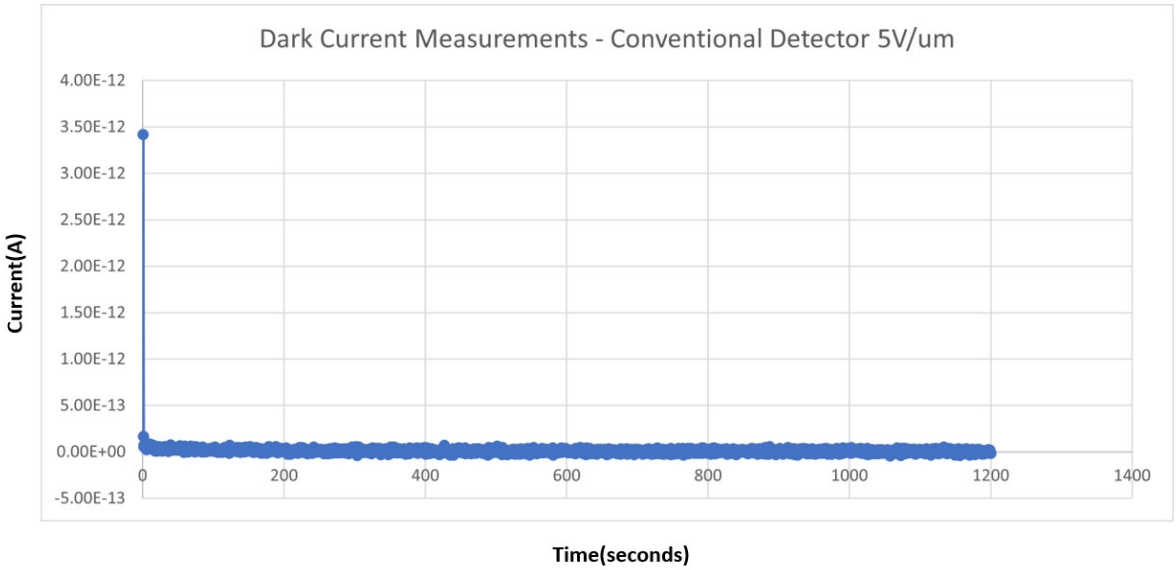

Figure 3.16: Dark Current Measurements for a conventional X-ray detector

conventional detector. However, it has been proven through simulations that increasing the electric field would also increase the output signal amplitude.It is to be noted that all the results for the unipolar charge sensing detector here are given when the grid voltage was at 0V.

It was not possible to test the device with an applied voltage on the grid electrodes as the voltage supply attached to the grid electrode would trip notifying a large amount of current flowing in through the grid electrodes to the device. To check and verify why this was happening we performed scanning electron microscopy on to our samples to see the reason behind it. It was noted in the figures below that some of the pixel strucutres were missing the PI layer on top of the collecting electrode. We discovered that this happened due to the fact that when we wanted to etch the PI on the signal tracks we didn't use the metal mask to protect the PI layer on top of the pixel as we didn't have a photomask for patterning the RIE metal mask. Hence once we were doing the RIE etch to etch away the

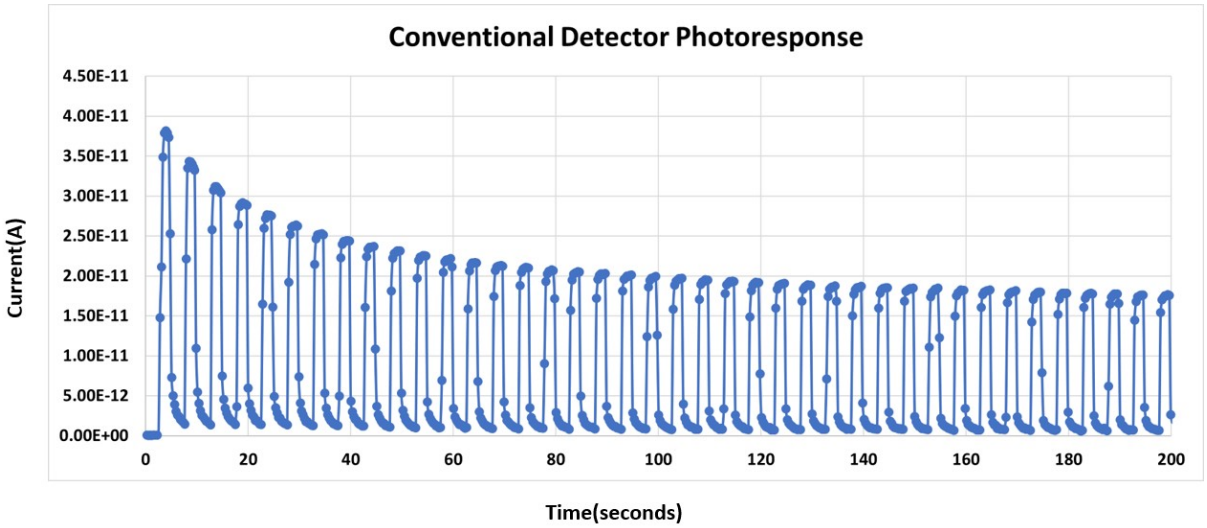

Figure 3.17: Photocurrent response for a conventional X-ray detector

PI layer on the signal tracks the oxygen plasma used for RIE etch also went through to the pixel electrodes and etched the PI on top of some of the pixel electrodes. Since the PI layer on top of the pixel electrode also served as an insulator to prevent charge injection from the grid layer to the photoconductor and collecting pixel electrode. All the grid electrodes in our design are connected together which allowed excess amount of charge to easily flow through the grid electrode towards the device causing the voltage supply to trip. The figure 3.21 below shows how a pixel electrode should be covered with the polyimide layer to help prevent any charge being injected in to the device through the grid electrode. The figure 3.22 to 3.24 show some of the pixel electrode with etched polyimide layer and some covered with polyimide layer in separate rows.

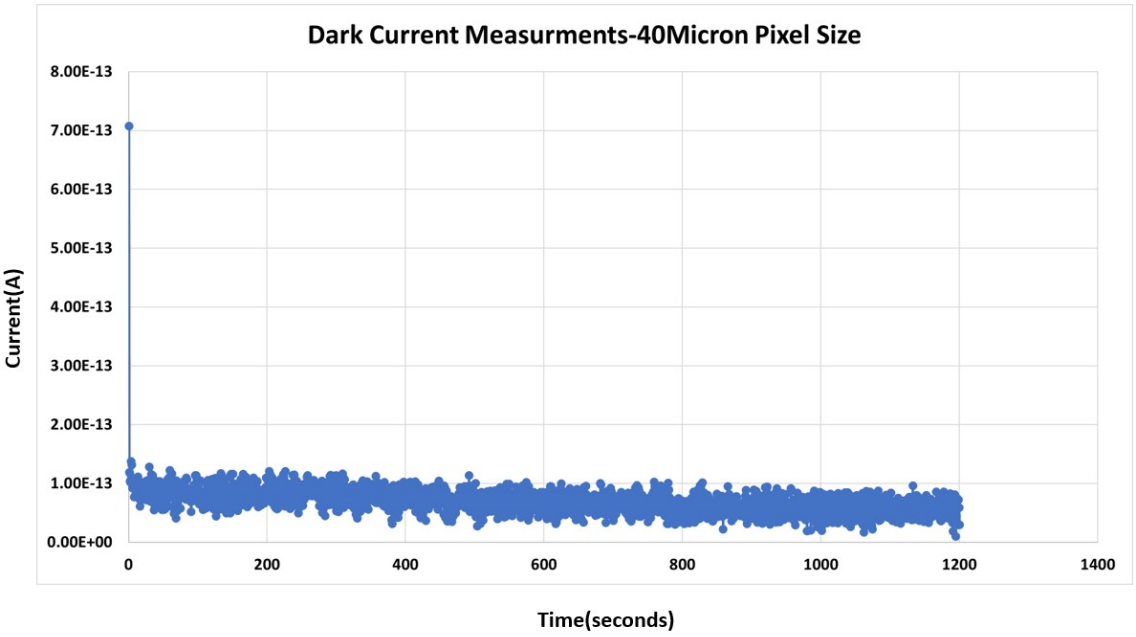

Figure 3.18: Dark Current Measurements for a 40um Pixel Size Unipolar Charge Sensing Detector.

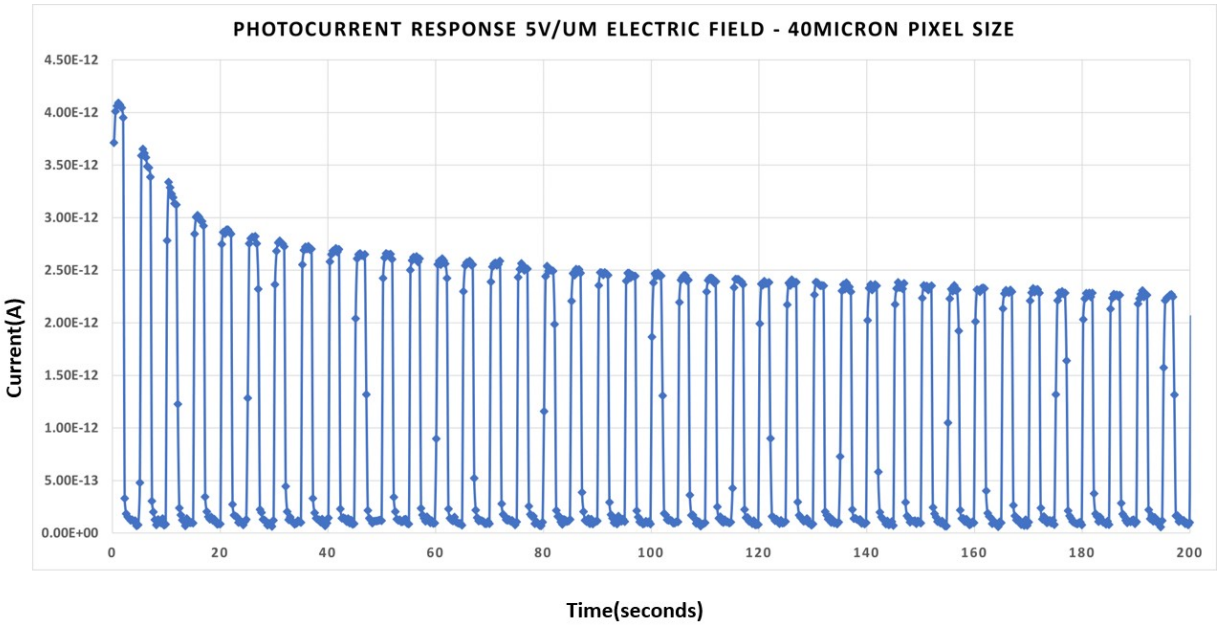

Figure 3.19: Photocurrent Response for the 40um Pixel Size unipolar charge sensing detector.

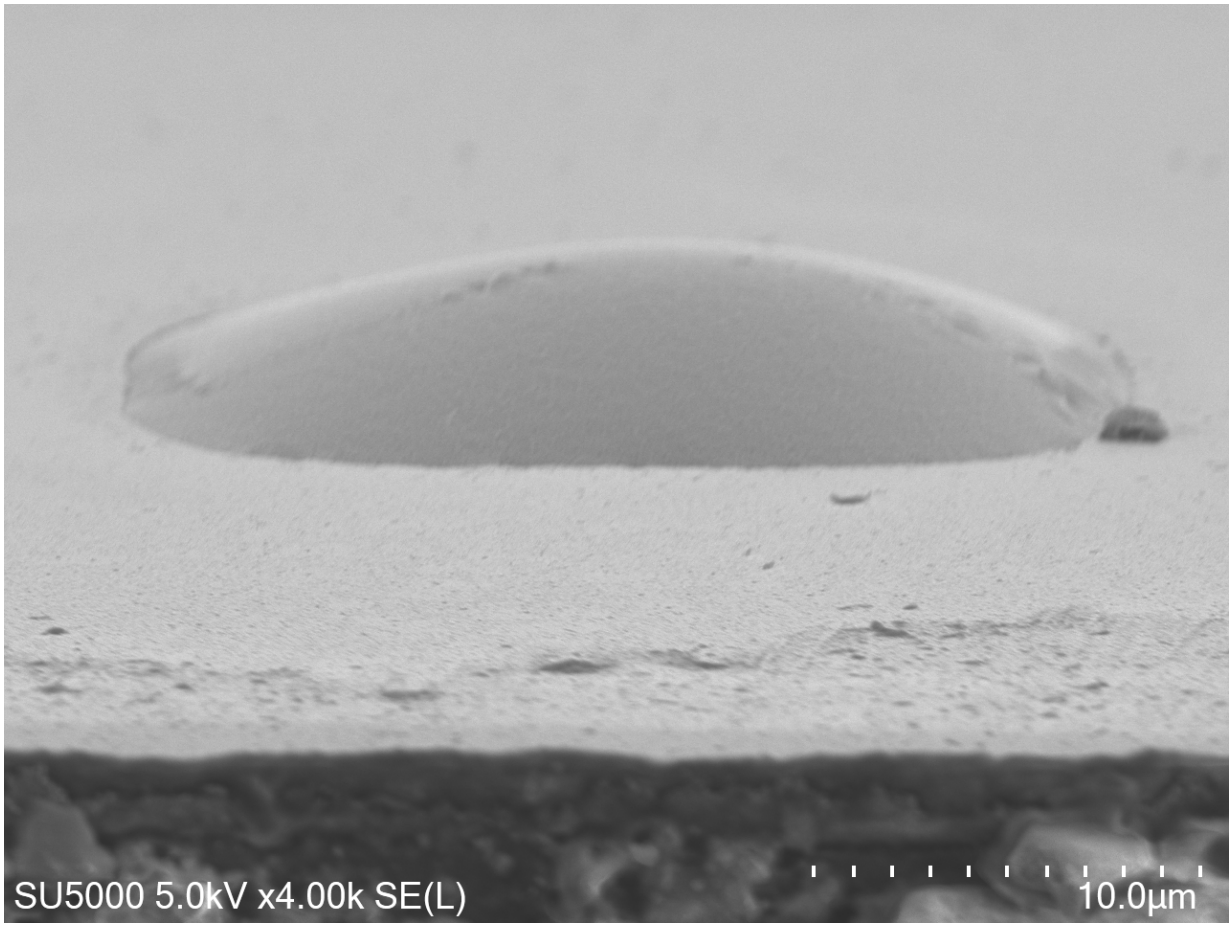

Figure 3.20: SEM image of a single Pixel Electrode in the fabricated device covered with poliyimde.

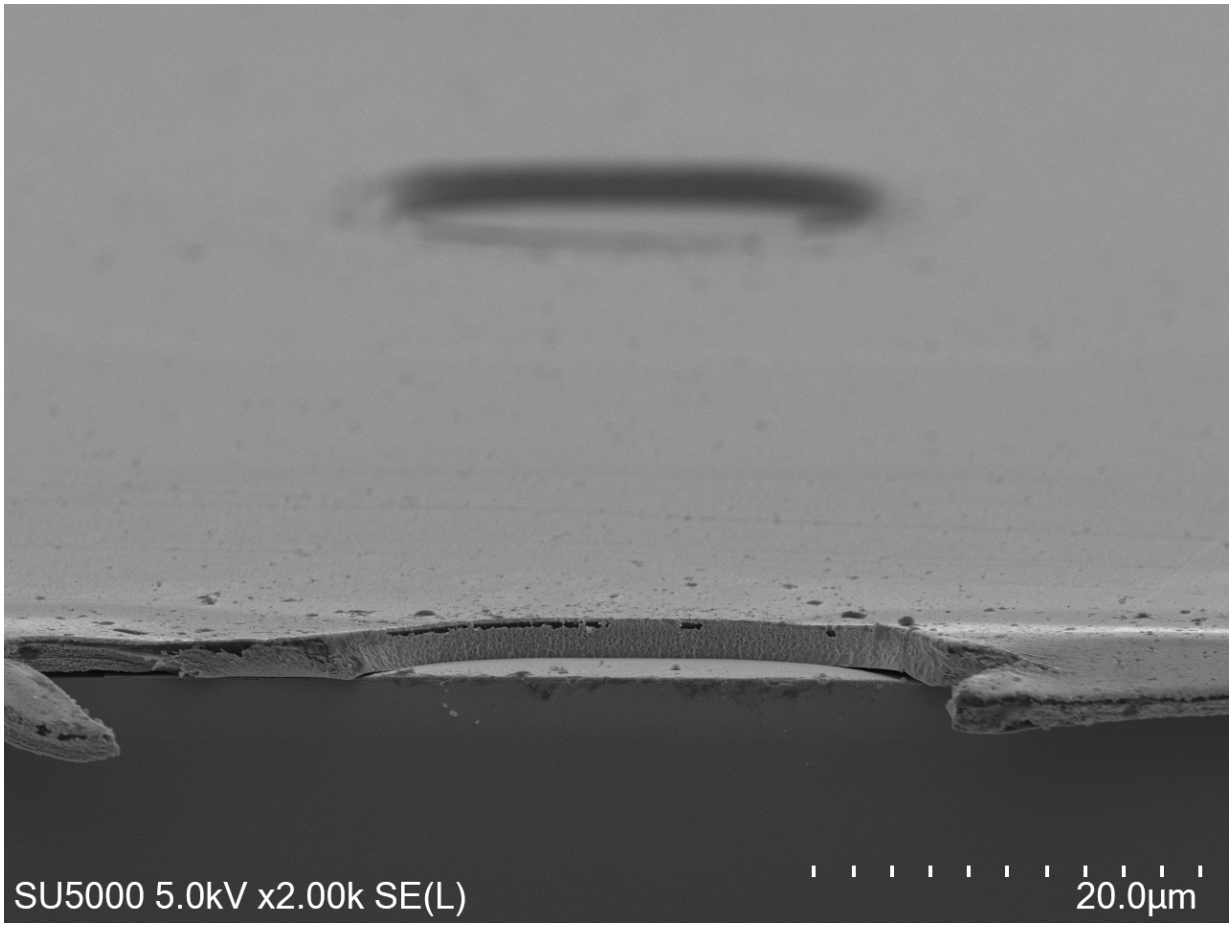

Figure 3.21: SEM image of a single Pixel Electrode in the fabricated device shown with etched Polyimide.

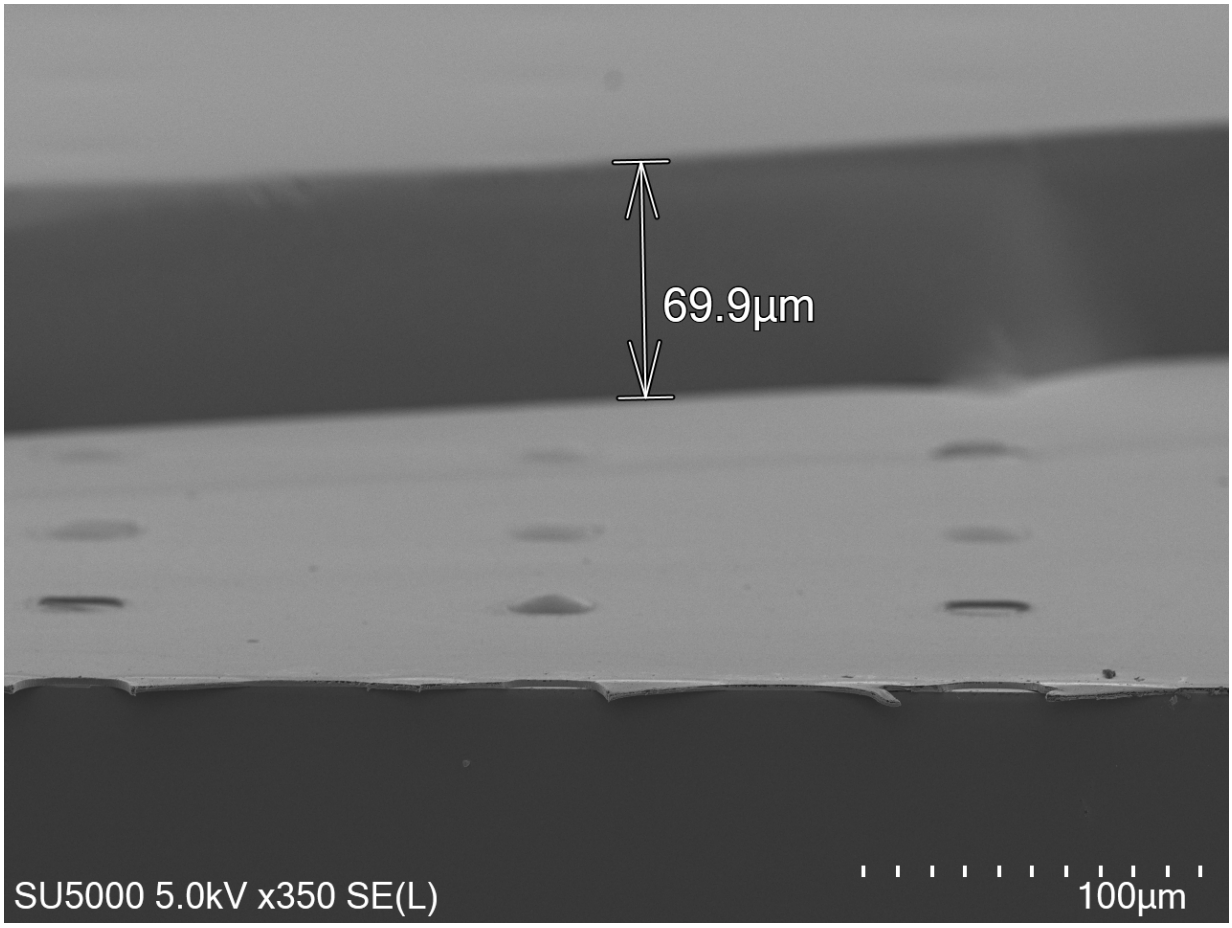

Figure 3.22: SEM image of a single Pixel Electrode in the fabricated device covered with poliyimde and some pixel electrode shown with etched Polyimide.

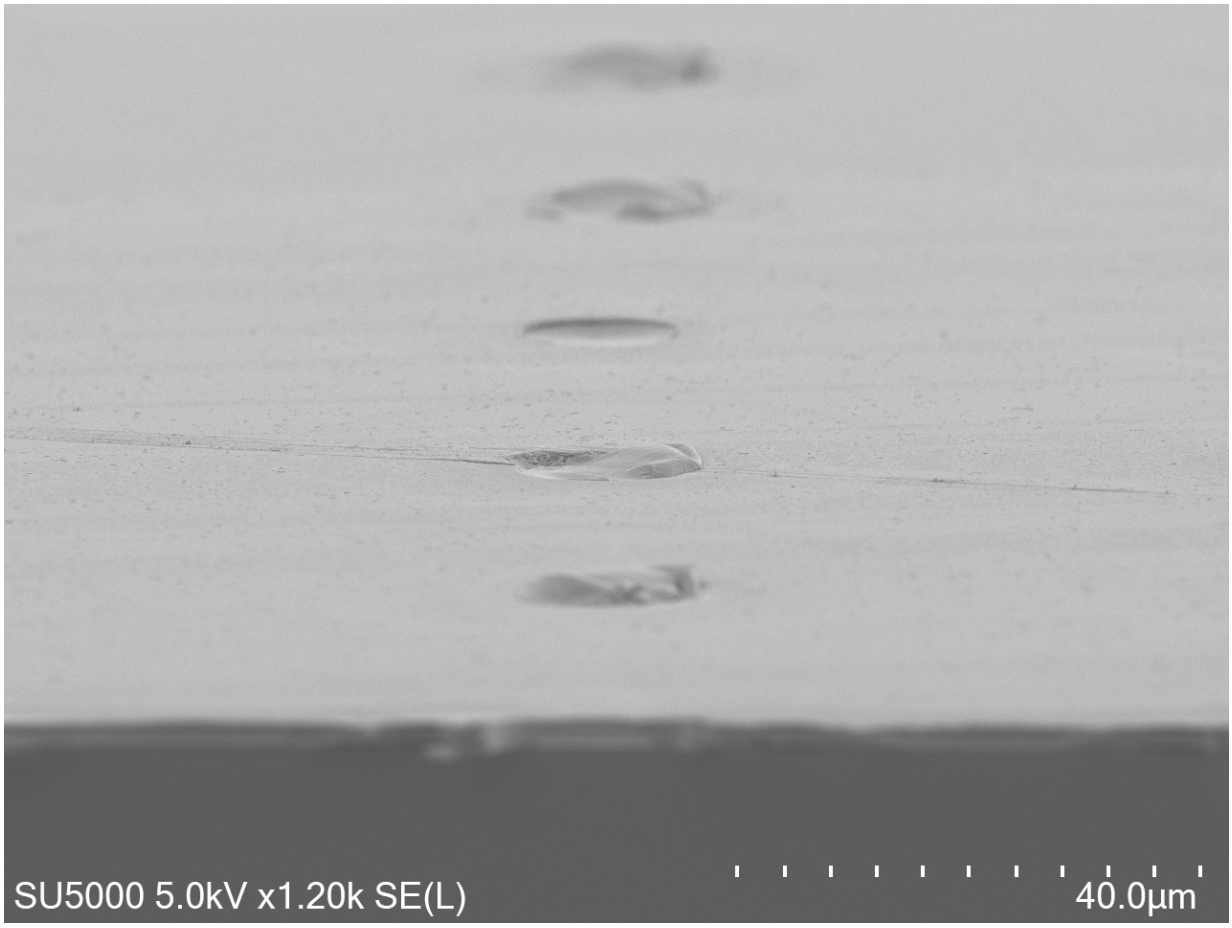

Figure 3.23: SEM image of a single Pixel Electrode in the fabricated device covered with poliyimde and some pixel electrode shown with etched Polyimide.

Chapter 4

Conclusions and Recommendations for Future Work

This work discussed the background knowledge related to x-ray imaging and detectors. It discussed the important factors such as sensitivity, dark current, photocurrent lag and ghosting that are important for designing x-ray detectors. This thesis presented the design of a unipolar charge sensing detector that can be used for X-ray photon counting with improved resolution and charge collection efficiency and improved lag. The simulation results shows that the charge collection efficiency for the unipolar charge sensing structure is nearly independent of from the detector's thickness compared to a conventional detector whose charge collection efficiency degraded with increased thickness. This happens because of the grid structure creating a near-field effect near the collecting pixel electrode allowing the collection of holes, the fast moving charge in amorphous Selenium photoconductor. The Pulse height spectroscopy simulations were performed on the Xenos Software suite to analyze the performance of the designed unipolar charge sensing detectors, the results from the PHS simulations were then used to determine the energy resolution of the designed detectors which ranged from 5% to 2% for the designed pixel sizes ranging from 80 microns to 20 microns. These simulations were performed at a electric field of $10V/um$ and an energy source of 60keV, to achieve the above mentioned results.

This work further describes the process for fabrication steps taken to fabricate the unipolar charge sensing detector in the Giga-to-Nano lab at the university of Waterloo. The photomask was designed using the K-layout software tool and manufactured at the nanofabrication facility at the university of Alberta. The photomasks were designed keeping the pixel size for the detectors at 20 micron, 40 micron and 80 micron on a 5-inch square chrome-glass masks. The devices were fabricated on a 4-inch diameter Corning eagle XG glass substrate using several processes including photolithography, metal sputtering, spin coating, wet metal etching and reactive ion etching. Polyimide layer was used to collect the fast charge carriers i.e. holes from the A-Se photoconductive layer as PI over the years have proven to be a good material for hole conduction and proven compatibility during fabrication with amorphous selenium. During characterization of the device, the voltage supply attached to the grid metal electrodes tripped whenever a voltage was applied on to the grid metal electrodes. The device samples were analyzed using the scanning electron microscope to investigate the cause of the problem. It was noted that the sample had non-uniform coating of polyimide layer between the photoconductor and grid electrode which happened during an RIE-etching process to uncover the signal tracks resulting in the PI layer over the pixel electrode to etch away. This resulted in excess charge to flow through the gate electrodes to the photoconductor and the collecting electrode creating a short circuit configuration and causing the voltage supply to trip. For future considerations to avoid making this mistake it is recommended to use an to deposit an aluminum metal layer and pattern it using a photomask to protect the poliyimide layer on top of the pixel electrodes.

Commercial medical imaging detectors have successfully utilized a-Se detectors due to their exceptional high spatial resolution. However, the photon-to-charge conversion energy required for amorphous selenium is significantly lower, by one order of magnitude, compared to direct conversion materials like CdTe or PbO when operating in a practical bias electric field of $10V/m$. It is desirable to develop a selenium imaging detector that can achieve avalanche gain. Previous studies have demonstrated that an avalanche gain can be achieved with a-Se through impact ionization under an applied field exceeding $90V/m$. However, one of the challenges lies in maintaining a lower dark current while operating

the detector at this applied field.By dividing the selenium detection layer into two distinct regions, namely a low-field charge absorption and drift region, and a high-field region utilizing additional grid structures, it becomes possible to achieve avalanche gain. Over the past few years, numerous research groups have explored this particular configuration and its variations for partitioning the selenium field, aiming to enhance charge collection and gain. The fabrication of such grid structures necessitates the use of insulating materials with a high dielectric strength to prevent electrical breakdown hotspots. Moreover, the electric field strength within the gain region is non-uniform, with stronger fields near the well's walls and weaker fields at the center of the well or trough. Image charges originating from different locations within the bulk material will drift along the field lines, ultimately reaching the avalanche gain region. Due to the non-uniform distribution of field strength across the gain region, even charges generated from the same pixel may exhibit different levels of avalanche gain. As the gain factor rapidly increases above the threshold field, the resulting non-uniform gain distribution can introduce significant image noise, particularly in applications involving low radiation doses. To stabilize the avalanche gain and mitigate issues such as run-away avalanches or excessive noise near the avalanche threshold potential, it becomes necessary to implement a negative feedback circuit.

References

[1] A. Camlica, "Device architectures for improved temporal response with amorphous selenium radiation detectors," 2019.

[2] F. J. Jimenez, "Comprehensive simulation of sputter deposition," Ph.D. dissertation, University of Alberta, 2012.

[3] S. Kasap, J. B. Frey, G. Belev, O. Tousignant, H. Mani, L. Laperriere, A. Reznik, and J. A. Rowlands, "Amorphous selenium and its alloys from early xeroradiography to high resolution x-ray image detectors and ultrasensitive imaging tubes: Amorphous se from early xeroradiography to high resolution x-ray image detectors," vol. 246, no. 8, pp. 1794–1805. [Online]. Available: https://onlinelibrary.wiley.com/doi/10.1002/pssb.200982007

[4] S. Abbaszadeh, "Indirect conversion amorphous selenium photodetectors for medical imaging applications," 2014.

[5] A. Sultana, A. Reznik, K. S. Karim, and J. A. Rowlands, "Design and feasibility of active matrix flat panel detector using avalanche amorphous selenium for protein crystallography: Flat panel detector protein crystallography using a-sia-se," vol. 35, no. 10, pp. 4324–4332. [Online]. Available: http://doi.wiley.com/10.1118/1.2975227

[6] A. Sultana, K. S. Karim, and J. A. Rowlands, "The effect of K- fluorescence reabsorption of selenium on the performance of an imaging detector for protein crystallography," vol. 6. [Online]. Available: https://onlinelibrary.wiley.com/doi/10.1002/pssc.200881346

[7] E. L. Gingold, D. L. Y. Lee, L. S. Jeromin, B. G. Rodricks, M. G. Hoffberg, and C. L. Williams, "Development of a novel high-resolution direct conversion x-ray detector," J. T. Dobbins III and J. M. Boone, Eds., p. 185. [Online]. Available: http://proceedings.spiedigitallibrary.org/proceeding.aspx?doi=10.1117/12.384492

[8] S. Kasap, J. B. Frey, G. Belev, O. Tousignant, H. Mani, J. Greenspan, L. Laperriere, O. Bubon, A. Reznik, G. DeCrescenzo, K. S. Karim, and J. A. Rowlands, "Amorphous and polycrystalline photoconductors for direct conversion flat panel x-ray image sensors," vol. 11, no. 5, pp. 5112–5157. [Online]. Available: http://www.mdpi.com/1424-8220/11/5/5112

[9] E. Samei and M. J. Flynn, "An experimental comparison of detector performance for direct and indirect digital radiography systems," vol. 30, no. 4, pp. 608–622. [Online]. Available: http://doi.wiley.com/10.1118/1.1561285

[10] J. A. Rowlands, W. G. Ji, W. Zhao, and D. L. Y. Lee, "Direct-conversion flat-panel x-ray imaging: reduction of noise by presampling filtration," J. T. Dobbins III and J. M. Boone, Eds., p. 446. [Online]. Available: http://proceedings.spiedigitallibrary.org/proceeding.aspx?doi=10.1117/12.384519

[11] S. Kasap and J. Rowlands, "Direct-conversion flat-panel x-ray image sensors for digital radiography," vol. 90, no. 4, pp. 591–604. [Online]. Available: http://ieeexplore.ieee.org/document/1002529/

[12] B. T. Polischuk, Z. Shukri, A. Legros, and H. Rougeot, "Selenium direct-converter structure for static and dynamic x-ray detection in medical imaging applications," J. T. Dobbins III and J. M. Boone, Eds., p. 494. [Online]. Available: http://proceedings.spiedigitallibrary.org/proceeding.aspx?doi=10.1117/12.317051

[13] S. Tokuda, H. Kishihara, S. Adachi, T. Sato, Y. Izumi, O. Teranuma, Y. Yamane, and S. Yamada, "Large-area deposition of a polycrystalline CdZnTe film and its applicability to x-ray panel detectors with superior sensitivity," L. E. Antonuk and M. J. Yaffe, Eds., pp. 30–41. [Online]. Available: http://proceedings.spiedigitallibrary.org/proceeding.aspx?articleid=879141

[14] S. Adachi, N. Hori, K. Sato, S. Tokuda, T. Sato, K. Uehara, Y. Izumi, H. Nagata, Y. Yoshimura, and S. Yamada, "Experimental evaluation of a-se and CdTe flat-panel x-ray detectors for digital radiography and fluoroscopy," J. T. Dobbins III and J. M. Boone, Eds., p. 38. [Online]. Available: http://proceedings.spiedigitallibrary.org/proceeding.aspx?doi=10.1117/12.384511

[15] W. C. Barber, E. Nygard, J. C. Wessel, N. Malakhov, G. Wawrzyniak, N. E. Hartsough, T. Gandhi, and J. S. Iwanczyk, "Fast photon counting CdTe detectors for diagnostic clinical CT: dynamic range, stability, and temporal response," p. 76221E. [Online]. Available: http://proceedings.spiedigitallibrary.org/proceeding.aspx?doi=10.1117/12.844669

[16] P. M. Shikhaliev, S. G. Fritz, and J. W. Chapman, "Photon counting multienergy x-ray imaging: Effect of the characteristic x rays on detector performance: Photon counting x-ray imaging: Effect of characteristic x rays," vol. 36, no. 11, pp. 5107–5119. [Online]. Available: http://doi.wiley.com/10.1118/1.3245875

[17] S. Kasap, M. Zahangir Kabir, and J. Rowlands, "Recent advances in x-ray photoconductors for direct conversion x-ray image detectors," vol. 6, no. 3, pp. 288–292. [Online]. Available: https://linkinghub.elsevier.com/retrieve/pii/S1567173905002415

[18] R. E. Tallman, B. Weinstein, A. Reznik, M. Kubota, K. Tanioka, and J. Rowlands, "Photo-crystallization in a-se imaging targets: Raman studies of competing effects," vol. 354, no. 40, pp. 4577–4581. [Online]. Available: https://linkinghub.elsevier.com/retrieve/pii/S0022309308003591

[19] K. S. Kim and D. Turnbull, "Crystallization of amorphous selenium films. II. photo and impurity effects," vol. 45, no. 8, pp. 3447–3452. [Online]. Available: http://aip.scitation.org/doi/10.1063/1.1663799

[20] B. Fogal, R. E. Johanson, G. Belev, S. O'Leary, and S. Kasap, "X-ray induced effects in stabilized a-se x-ray photoconductors," vol. 299-302, pp. 993–997. [Online]. Available: https://linkinghub.elsevier.com/retrieve/pii/S0022309301010651

[21] S. O. Kasap, K. V. Koughia, B. Fogal, G. Belev, and R. E. Johanson, "The influence of deposition conditions and alloying on the electronic properties of amorphous selenium," vol. 37, no. 7, pp. 789–794. [Online]. Available: http://link.springer.com/10.1134/1.1592851

[22] W. Zhao, W. G. Ji, A. Debrie, and J. A. Rowlands, "Imaging performance of amorphous selenium based flat-panel detectors for digital mammography: Characterization of a small area prototype detector," vol. 30, no. 2, pp. 254–263. [Online]. Available: http://doi.wiley.com/10.1118/1.1538233

[23] S. O. Kasap and J. A. Rowlands, "Review x-ray photoconductors and stabilized a-se for direct conversion digital ¯at-panel x-ray image- detectors."

[24] G. S. Belev, B. Fogal, K. V. Koughia, R. E. Johanson, and S. O. Kasap, "Dependence of charge-carrier ranges in stabilized a-se on preparation conditions and alloying."

[25] G. Chotas, E. Floyd, and E. Ravin, "and instrumentation digital."

[26] S. O. Kasap, "CHARGE TRANSPORT IN SELENIUM BASED AMORPHOUS XEROGRAPHIC PHOTORECEPTORS."

[27] A. H. Goldan, J. A. Rowlands, O. Tousignant, and K. S. Karim, "Unipolar time-differential charge sensing in non-dispersive amorphous solids," vol. 113, no. 22, p. 224502. [Online]. Available: http://aip.scitation.org/doi/10.1063/1.4807292

[28] S. Abbaszadeh, S. Ghaffari, S. Siddiquee, M. Z. Kabir, and K. S. Karim, "Characterization of lag signal in amorphous selenium detectors," vol. 63, no. 2, pp. 704–709. [Online]. Available: http://ieeexplore.ieee.org/document/7372415/

[29] S. Siddiquee and M. Z. Kabir, "Modeling of photocurrent and lag signals in amorphous selenium x-ray detectors," vol. 33, no. 4, p. 041514. [Online]. Available: http://avs.scitation.org/doi/10.1116/1.4923037

[30] J. F. Hainfeld, F. A. Dilmanian, D. N. Slatkin, and H. M. Smilowitz, "Radiotherapy enhancement with gold nanoparticles," *Journal of pharmacy and pharmacology*, vol. 60, no. 8, pp. 977–985, 2008.

[31] M. F. Stone, W. Zhao, B. V. Jacak, P. O'Connor, B. Yu, and P. Rehak, "The x-ray sensitivity of amorphous selenium for mammography," *Medical Physics*, vol. 29, no. 3, pp. 319–324, 2002.

[32] W. Que and J. Rowlands, "X-ray imaging using amorphous selenium: Inherent spatial resolution," *Medical physics*, vol. 22, no. 4, pp. 365–374, 1995.

[33] G. S. Belev, *Electrical properties of amorphous selenium based photoconductive devices for application in X-ray image detectors*, 2007, vol. 68, no. 09.

[34] G. Belev, S. Kasap, J. Rowlands, D. Hunter, and M. Yaffe, "Dependence of the electrical properties of stabilized a-se on the preparation conditions and the development of a double layer x-ray detector structure," *Current Applied Physics*, vol. 8, no. 3-4, pp. 383–387, 2008.

[35] R. E. Johanson, S. O. Kasap, J. Rowlands, and B. Polischuk, "Metallic electrical contacts to stabilized amorphous selenium for use in x-ray image detectors," *Journal of non-crystalline solids*, vol. 227, pp. 1359–1362, 1998.

[36] S. Kasap and G. Belev, "Progress in the science and technology of direct conversion x-ray image detectors: The development of a double layer a-se based detector," *Journal of Optoelectronics and advanced materials*, vol. 9, no. 1, pp. 1–10, 2007.

[37] S. A. Mahmood and M. Z. Kabir, "Dark current mechanisms in stabilized amorphous selenium based n-i detectors for x-ray imaging applications," vol. 29, no. 3, p. 031603. [Online]. Available: http://avs.scitation.org/doi/10.1116/1.3580902

[38] M. Z. Kabir, "Dark current mechanisms in amorphous selenium-based photoconductive detectors: an overview and re-examination," vol. 26, no. 7, pp. 4659–4667. [Online]. Available: http://link.springer.com/10.1007/s10854-015-2675-2

[39] S. Abbaszadeh, N. Allec, and K. Karim, "Characterization of low dark-current lateral amorphous-selenium metal-semiconductor-metal photodetectors," vol. 13, no. 5, pp. 1452–1458. [Online]. Available: http://ieeexplore.ieee.org/document/6384644/

[40] S. Abbaszadeh, N. Allec, S. Ghanbarzadeh, U. Shafique, and K. S. Karim, "Investigation of hole-blocking contacts for high-conversion-gain amorphous selenium detectors for x-ray imaging," vol. 59, no. 9, pp. 2403–2409. [Online]. Available: http://ieeexplore.ieee.org/document/6237521/

[41] A. Camlica, M. Z. Kabir, J. Liang, P. M. Levine, D. L. Lee, and K. S. Karim, "Use of pulse-height spectroscopy to characterize the hole conduction mechanism of a polyimide blocking layer used in amorphous-selenium radiation detectors," *IEEE Transactions on Electron Devices*, vol. 67, no. 2, pp. 633–639, 2020.

[42] A. El-Falou, A. Camlica, R. Mohammadi, P. M. Levine, and K. S. Karim, "A monolithic amorphous-selenium/cmos single-photon-counting x-ray detector," *IEEE Transactions on Electron Devices*, vol. 68, no. 4, pp. 1746–1752, 2021.

[43] A. Camlica, D. Lee, H. Jang, M. Z. Kabir, and K. Karim, "Energy resolution of amorphous selenium detectors: conventional vs unipolar charge sensing," in *Medical Imaging 2022: Physics of Medical Imaging*. SPIE, 2022, p. PC120310G.

[44] S. Kasap, "X-ray sensitivity of photoconductors: application to stabilized a-se," *Journal of Physics D: Applied Physics*, vol. 33, no. 21, p. 2853, 2000.

[45] H. G. Chotas, C. E. Floyd Jr, and C. E. Ravin, "Memory artifact related to selenium-based digital radiography systems." *Radiology*, vol. 203, no. 3, pp. 881–883, 1997.

[46] O. Tousignant, Y. Demers, L. Laperriere, H. Mani, P. Gauthier, and J. Leboeuf, "Spatial and temporal image characteristics of a real-time large area a-se x-ray detector," in *Medical Imaging 2005: Physics of Medical Imaging*, vol. 5745. SPIE, 2005, pp. 207–215.

[47] C. Haugen, S. Kasap, and J. Rowlands, "X-ray irradiation induced bulk space charge in stabilized a-se x-ray photoconductors," *Journal of applied physics*, vol. 84, no. 10, pp. 5495–5501, 1998.

[48] S. Kasap, B. Fogal, M. Zahangir Kabir, R. E. Johanson, and S. K. O'Leary, "Recombination of drifting holes with trapped electrons in stabilized a-se photoconductors: Langevin recombination," *Applied physics letters*, vol. 84, no. 11, pp. 1991–1993, 2004.

[49] K. Taguchi and J. S. Iwanczyk, "Vision 20/20: Single photon counting x-ray detectors in medical imaging: Vision 20/20: Photon counting detectors," vol. 40, no. 10, p. 100901. [Online]. Available: http://doi.wiley.com/10.1118/1.4820371

[50] J. Giersch, D. Niederlöhner, and G. Anton, "The influence of energy weighting on x-ray imaging quality," vol. 531, no. 1, pp. 68–74. [Online]. Available: https://linkinghub.elsevier.com/retrieve/pii/S0168900204010800

[51] J. Tanguay, H. K. Kim, and I. A. Cunningham, "The role of x-ray swank factor in energy-resolving photon-counting imaging: Swank factor in energy-resolving photon-counting imaging," vol. 37, no. 12, pp. 6205–6211. [Online]. Available: http://doi.wiley.com/10.1118/1.3512794

[52] E. Fredenberg, M. Hemmendorff, B. Cederström, M. Åslund, and M. Danielsson, "Contrast-enhanced spectral mammography with a photon-counting detector: Contrast-enhanced spectral mammography with a photon-counting detector," vol. 37, no. 5, pp. 2017–2029. [Online]. Available: http://doi.wiley.com/10.1118/1.3371689

[53] J. M. Lewin, P. K. Isaacs, V. Vance, and F. J. Larke, "Dual-energy contrast-enhanced digital subtraction mammography: Feasibility," vol. 229, no. 1, pp. 261–268. [Online]. Available: http://pubs.rsna.org/doi/10.1148/radiol.2291021276

[54] P. M. Shikhaliev, "Projection x-ray imaging with photon energy weighting: experimental evaluation with a prototype detector," vol. 54, no. 16, pp. 4971–4992.

[Online]. Available: https://iopscience.iop.org/article/10.1088/0031-9155/54/16/009

[55] M. Locker, P. Fischer, S. Krimmel, H. Kruger, M. Lindner, K. Nakazawa, T. Takahashi, and N. Wermes, "Single photon counting x-ray imaging with si and CdTe single chip pixel detectors and multichip pixel modules," vol. 51, no. 4, pp. 1717–1723. [Online]. Available: http://ieeexplore.ieee.org/document/1323757/

[56] K. Spartiotis, A. Leppänen, T. Pantsar, J. Pyyhtiä, P. Laukka, K. Muukkonen, O. Männistö, J. Kinnari, and T. Schulman, "A photon counting CdTe gamma- and x-ray camera," vol. 550, no. 1, pp. 267–277. [Online]. Available: https://linkinghub.elsevier.com/retrieve/pii/S0168900205012362

[57] Cheng Xu, M. Danielsson, and H. Bornefalk, "Evaluation of energy loss and charge sharing in cadmium telluride detectors for photon-counting computed tomography," vol. 58, no. 3, pp. 614–625. [Online]. Available: http://ieeexplore.ieee.org/document/5740625/

[58] R. Ballabriga, M. Campbell, E. H. M. Heijne, X. Llopart, and L. Tlustos, "The medipix3 prototype, a pixel readout chip working in single photon counting mode with improved spectrometric performance," vol. 54, no. 5, pp. 1824–1829. [Online]. Available: http://ieeexplore.ieee.org/document/4346690/

[59] C. Szeles, "CdZnTe and CdTe materials for x-ray and gamma ray radiation detector applications," vol. 241, no. 3, pp. 783–790. [Online]. Available: https://onlinelibrary.wiley.com/doi/10.1002/pssb.200304296

[60] C. Scheiber, "CdTe and CdZnTe detectors in nuclear medicine," vol. 448, no. 3, pp. 513–524. [Online]. Available: https://linkinghub.elsevier.com/retrieve/pii/S0168900200002825

[61] M. Bissonnette, M. Hansroul, E. Masson, S. Savard, S. Cadieux, P. Warmoes, D. Gravel, J. Agopyan, B. Polischuk, W. Haerer *et al.*, "Digital breast tomosyn-

thesis using an amorphous selenium flat panel detector," in *Medical Imaging 2005: Physics of Medical Imaging*, vol. 5745. SPIE, 2005, pp. 529–540.

[62] B. Zhao and W. Zhao, "Imaging performance of an amorphous selenium digital mammography detector in a breast tomosynthesis system: Imaging performance of a-se detector in breast tomosynthesis," vol. 35, no. 5, pp. 1978–1987. [Online]. Available: http://doi.wiley.com/10.1118/1.2903425

[63] S. K. Moore, "Better breast cancer detection," *Ieee Spectrum*, vol. 38, no. 5, pp. 50–54, 2001.

[64] I. M. Blevis, D. C. Hunt, and J. A. Rowlands, "Measurement of x-ray photogeneration in amorphous selenium," vol. 85, no. 11, pp. 7958–7963. [Online]. Available: http://aip.scitation.org/doi/10.1063/1.370615

[65] W. E. Spear, "Transit time measurements of charge carriers in amorphous selenium films," vol. 70, no. 7, pp. 669–675. [Online]. Available: https://iopscience.iop.org/article/10.1088/0370-1301/70/7/304

[66] K. Tanioka, J. Yamazaki, K. Shidara, K. Taketoshi, T. Kawamura, S. Ishioka, and Y. Takasaki, "An avalanche-mode amorphous selenium photoconductive layer for use as a camera tube target," *IEEE electron device letters*, vol. 8, no. 9, pp. 392–394, 1987.

[67] K. Tanioka, "High-gain avalanche rushing amorphous photoconductor (harp) detector," *Nuclear Instruments and Methods in Physics Research Section A: Accelerators, Spectrometers, Detectors and Associated Equipment*, vol. 608, no. 1, pp. S15–S17, 2009.

[68] J. Eskin, H. Barrett, and H. Barber, "Signals induced in semiconductor gamma-ray imaging detectors," *Journal of applied physics*, vol. 85, no. 2, pp. 647–659, 1999.

[69] J. D. Eskin, H. H. Barrett, and H. B. Barber, "Signals induced in semiconductor gamma-ray imaging detectors," vol. 85, no. 2, pp. 647–659. [Online]. Available: http://aip.scitation.org/doi/10.1063/1.369198

[70] P. N. Luke, "Single-polarity charge sensing in ionization detectors using coplanar electrodes," vol. 65, no. 22, pp. 2884–2886. [Online]. Available: http://aip.scitation.org/doi/10.1063/1.112523

[71] S. Ramo, "Currents induced by electron motion," vol. 27, no. 9, pp. 584–585. [Online]. Available: http://ieeexplore.ieee.org/document/1686997/

[72] W. Shockley, "Currents to conductors induced by a moving point charge," vol. 9, no. 10, pp. 635–636. [Online]. Available: http://aip.scitation.org/doi/10.1063/1.1710367

[73] O. Tousignant, M. Choquette, Y. Demers, L. Laperriere, J. Leboeuf, M. Honda, M. Nishiki, A. Takahashi, and A. Tsukamoto, "Progress report on the performance of real-time selenium flat-panel detectors for direct x-ray imaging," in *Medical Imaging 2002: Physics of Medical Imaging*, vol. 4682. SPIE, 2002, pp. 503–510.

[74] K. Karim, A. Nathan, J. Rowlands, and S. Kasap, "X-ray detector with on-pixel amplification for large area diagnostic medical imaging," *IEE Proceedings-Circuits, Devices and Systems*, vol. 150, no. 4, pp. 267–273, 2003.

[75] M. Simon, K.-J. Engel, B. Menser, X. Badel, and J. Linnros, "Challenges of pixelated scintillators in medical x-ray imaging," vol. 591, no. 1, pp. 291–295. [Online]. Available: https://linkinghub.elsevier.com/retrieve/pii/S0168900208004609

[76] J. G. Yorker, L. S. Jeromin, D. L. Lee, E. F. Palecki, K. P. Golden, and Z. Jing, "Characterization of a full-field digital mammography detector based on direct x-ray conversion in selenium," in *Medical Imaging 2002: Physics of Medical Imaging*, vol. 4682. SPIE, 2002, pp. 21–29.

[77] W. Que and J. A. Rowlands, "X-ray imaging using amorphous selenium: Inherent spatial resolution," vol. 22, no. 4, pp. 365–374. [Online]. Available: http://doi.wiley.com/10.1118/1.597471

[78] H.-K. Kim, I. A. Cunningham, Z. Yin, and G.-S. Cho, "On the development of digital radiography detectors: A review," *International Journal of Precision Engineering and Manufacturing*, vol. 9, no. 4, pp. 86–100, 2008.

[79] J. B. Frey, G. Belev, O. Tousignant, H. Mani, L. Laperriere, and S. O. Kasap, "Dark current in multilayer stabilized amorphous selenium based photoconductive x-ray detectors," vol. 112, no. 1, p. 014502. [Online]. Available: http://aip.scitation.org/doi/10.1063/1.4730135

[80] B. Zhao and W. Zhao, "Temporal performance of amorphous selenium mammography detectors: Temporal performance of amorphous selenium mammography detectors," vol. 32, no. 1, pp. 128–136. [Online]. Available: http://doi.wiley.com/10.1118/1.1827791

[81] A. Camlica, D. L. Lee, and K. S. Karim, "Increased temporal resolution of amorphous selenium detector using preferential charge sensing approach," in *Medical Imaging 2018: Physics of Medical Imaging*, vol. 10573. SPIE, 2018, pp. 1509–1518.

[82] K. Kikuchi, Y. Ohkawa, K. Miyakawa, T. Matsubara, K. Tanioka, M. Kubota, and N. Egami, "Hole-blocking mechanism in high-gain avalanche rushing amorphous photoconductor (HARP) film," vol. 8, no. 9, pp. 2800–2803. [Online]. Available: https://onlinelibrary.wiley.com/doi/10.1002/pssc.201084055

[83] J. Eskin, H. Barrett, H. Barber, and J. Woolfenden, "The effect of pixel geometry on spatial and spectral resolution in a CdZnTe imaging array," in *1995 IEEE Nuclear Science Symposium and Medical Imaging Conference Record*, vol. 1. IEEE, pp. 544–548. [Online]. Available: http://ieeexplore.ieee.org/document/504320/

[84] G. F. Knoll, *Radiation detection and measurement*. John Wiley & Sons, 2010.

[85] U. Fano, "Ionization yield of radiations. ii. the fluctuations of the number of ions," *Physical Review*, vol. 72, no. 1, p. 26, 1947.

[86] P. Rehak, J. Walton, E. Gatti, A. Longoni, M. Sanpietro, J. Kemmer, H. Dietl, P. Holl, R. Klanner, G. Lutz *et al.*, "Progress in semiconductor drift detectors," *Nuclear Instruments and Methods in Physics Research Section A: Accelerators, Spectrometers, Detectors and Associated Equipment*, vol. 248, no. 2-3, pp. 367–378, 1986.

[87] M. Schieber, A. Zuck, H. Gilboa, and G. Zentai, "Reviewing polycrystalline mercuric iodide x-ray detectors," *IEEE Transactions on Nuclear Science*, vol. 53, no. 4, pp. 2385–2391, 2006.

[88] P. R. Bennett, "Characterization of polycrystalline TlBr films for radiographic detectors."

[89] M.-s. Yun, S.-h. Cho, R. Lee, G.-w. Jang, Y.-s. Kim, W.-j. Shin, and S.-h. Nam, "Investigation of PbI $_2$ film fabricated by a new sedimentation method as an x-ray conversion material," vol. 49, no. 4, p. 041801. [Online]. Available: https://iopscience.iop.org/article/10.1143/JJAP.49.041801

[90] Q. Zhao, L. E. Antonuk, Y. El-Mohri, Y. Wang, H. Du, A. Sawant, Z. Su, and J. Yamamoto, "Performance evaluation of polycrystalline HgI2 photoconductors for radiation therapy imaging: Performance evaluation of polycrystalline HgI2 for MV imaging," vol. 37, no. 6, pp. 2738–2748. [Online]. Available: http://doi.wiley.com/10.1118/1.3416924

[91] S. Tokuda, H. Kishihara, S. Adachi, and T. Sato, "Preparation and characterization of polycrystalline CdZnTe ®lms for large-area, high-sensitivity x-ray detectors."

[92] M. Galanti, R. Gott, and J. F. Renaud, "A high resolution, high sensitivity channel plate image intensifier for use in particle spectrographs," vol. 42, no. 12, pp. 1818–1822. [Online]. Available: http://aip.scitation.org/doi/10.1063/1.1685013

[93] D. C. Hunt, O. Tousignant, and J. A. Rowlands, "Evaluation of the imaging properties of an amorphous selenium-based flat panel detector for digital fluoroscopy," vol. 31, no. 5, pp. 1166–1175. [Online]. Available: http://doi.wiley.com/10.1118/1.1707755

[94] E. Davis, "Optical absorption, transport and photoconductivity in amorphous selenium," vol. 4, pp. 107–116. [Online]. Available: https://linkinghub.elsevier.com/retrieve/pii/0022309370900268

[95] J. L. Hartke, "Drift mobilities of electrons and holes and space-charge-limited currents in amorphous selenium films," vol. 125, no. 4, pp. 1177–1192. [Online]. Available: https://link.aps.org/doi/10.1103/PhysRev.125.1177

[96] M. L. Benkhedir, M. Brinza, and G. J. Adriaenssens, "Electronic density of states in amorphous selenium," vol. 16, no. 44, pp. S5253–S5264. [Online]. Available: https://iopscience.iop.org/article/10.1088/0953-8984/16/44/022

[97] K. Koughia, Z. Shakoor, S. O. Kasap, and J. M. Marshall, "Density of localized electronic states in a-se from electron time-of-flight photocurrent measurements," vol. 97, no. 3, p. 033706. [Online]. Available: http://aip.scitation.org/doi/10.1063/1.1835560

[98] M. Abkowitz, "Density of states in a-se from combined analysis of xerographic potentials and transient transport data," vol. 58, no. 1, pp. 53–57. [Online]. Available: http://www.tandfonline.com/doi/abs/10.1080/09500838808214730

[99] M. Choquette, Y. Demers, Z. Shukri, O. Tousignant, K. Aoki, M. Honda, A. Takahashi, and A. Tsukamoto, "Performance of a real-time selenium-based x-ray detector for fluoroscopy," L. E. Antonuk and M. J. Yaffe, Eds., p. 501. [Online]. Available: http://proceedings.spiedigitallibrary.org/proceeding.aspx?doi=10.1117/12.430873

[100] A. Sultana, A. Reznik, K. S. Karim, and J. A. Rowlands, "Design and feasibility of active matrix flat panel detector using avalanche amorphous selenium for protein crystallography: Flat panel detector protein crystallography using a-sia-se," vol. 35, no. 10, pp. 4324–4332. [Online]. Available: http://doi.wiley.com/10.1118/1.2975227

[101] S. O. Kasap and C. Juhasz, "Time-of-flight drift mobility measurements on chlorine-doped amorphous selenium films," vol. 18, no. 4, pp. 703–720. [Online]. Available: https://iopscience.iop.org/article/10.1088/0022-3727/18/4/015

[102] S. M. Vaezi-Nejad, "Xerographic time of flight experiment for the determination of drift mobility in high resistivity semiconductors," vol. 62, no. 3, pp. 361–384. [Online]. Available: http://www.tandfonline.com/doi/abs/10.1080/00207218708920988

[103] H. Scher and E. W. Montroll, "Anomalous transit-time dispersion in amorphous solids," vol. 12, no. 6, pp. 2455–2477. [Online]. Available: https://link.aps.org/doi/10.1103/PhysRevB.12.2455

[104] G. Pfister, "Hopping transport in a molecularly doped organic polymer," vol. 16, no. 8, pp. 3676–3687. [Online]. Available: https://link.aps.org/doi/10.1103/PhysRevB.16.3676

[105] I. M. Blevis, D. C. Hunt, and J. A. Rowlands, "Measurement of x-ray photogeneration in amorphous selenium," vol. 85, no. 11, pp. 7958–7963. [Online]. Available: http://aip.scitation.org/doi/10.1063/1.370615

[106] K. C. Young, "Recent developments in digital mammography," vol. 18, no. 2, pp. 68–74. [Online]. Available: http://www.birpublications.org/doi/10.1259/imaging/24202756

[107] J. A. Rowlands, G. DeCrescenzo, and N. Araj, "X-ray imaging using amorphous selenium: Determination of x-ray sensitivity by pulse height spectroscopy: X-ray imaging using amorphous selenium," vol. 19, no. 4, pp. 1065–1069. [Online]. Available: http://doi.wiley.com/10.1118/1.596825

[108] M. Schieber, A. Zuck, H. Gilboa, and G. Zentai, "Reviewing polycrystalline mercuric iodide x-ray detectors," vol. 53, no. 4, pp. 2385–2391. [Online]. Available: http://ieeexplore.ieee.org/document/1684115/

[109] S. Mahmood, M. Kabir, O. Tousignant, H. Mani, J. Greenspan, and P. Botka, "Dark current in multilayer amorphous selenium x-ray imaging detectors," *Applied Physics Letters*, vol. 92, no. 22, p. 223506, 2008.

[110] B. T. Polischuk, Z. Shukri, A. Legros, and H. Rougeot, "Selenium direct-converter structure for static and dynamic x-ray detection in medical imaging applications," in *Medical Imaging 1998: Physics of Medical Imaging*, vol. 3336. SPIE, 1998, pp. 494–504.

[111] M. Z. Kabir, "Modeling of x-ray photoconductors for x-ray image detectors," Ph.D. dissertation, University of Saskatchewan, 2005.

[112] J. M. Boone, M. H. Buonocore, and V. N. Cooper III, "Monte carlo validation in diagnostic radiological imaging," *Medical physics*, vol. 27, no. 6, pp. 1294–1304, 2000.